Phase Space Density Analysis of Outer Radiation Belt Electron Energization and Loss during Geoeffective and Nongeoeffective Sheath Regions

Milla M. H. Kalliokoski[1], Emilia Kilpua[1], Adnane Osmane[1], Allison N Jaynes[2], Drew L. Turner[3], Harriet George[1], Lucile Turc[1], and Minna Palmroth[1]

[1]University of Helsinki
[2]University of Iowa
[3]The Johns Hopkins University Applied Physics Laboratory

November 24, 2022

Abstract

Coronal mass ejection driven sheath regions are one of the key drivers of drastic outer radiation belt responses. The response can however be significantly different based on the sheath properties and associated inner magnetospheric wave activity. We performed here two case studies on the effects of sheaths on outer belt electrons of various energies using data from the Van Allen Probes. One sheath caused a major geomagnetic disturbance and the other one had only a minor impact. We especially investigated phase space density of high-energy electrons to determine the dominant energization and loss processes taking place during the events. Both sheaths produced substantial variation in the electron fluxes from tens of kiloelectronvolts up to ultrarelativistic energies. The responses were however almost the opposite: the geoeffective sheath led to enhancement, while the nongeoeffective one caused a depletion throughout most of the outer belt. The case studies highlight that both inward and outward radial transport driven by ultra-low frequency waves, combined with compression of the magnetopause, played an important role in governing electron dynamics during these sheaths. Chorus waves also likely caused a local peak in phase space density, leading to the energization of the ultrarelativistic population during the geoeffective event. The occurrence of chorus waves was based on measurements of precipitating and trapped fluxes by low-altitude Polar Operational Environmental Satellites. The distinct responses and different mechanisms in action during these events are related to differing levels of substorm activity and timing of the peaked solar wind dynamic pressure in the sheaths.

Phase Space Density Analysis of Outer Radiation Belt Electron Energization and Loss during Geoeffective and Nongeoeffective Sheath Regions

Milla M. H. Kalliokoski[1], Emilia K. J. Kilpua[1], Adnane Osmane[1], Allison N. Jaynes[2], Drew L. Turner[3], Harriet George[1], Lucile Turc[1], Minna Palmroth[1,4]

[1]Department of Physics, University of Helsinki, Helsinki, Finland
[2]Department of Physics and Astronomy, University of Iowa, Iowa City, Iowa, USA
[3]Johns Hopkins University Applied Physics Laboratory, Laurel, Maryland, USA
[4]Space and Earth Observation Centre, Finnish Meteorological Institute, Helsinki, Finland

Key Points:

- Opposite outer belt response to geoeffective and nongeoeffective sheaths, and physical mechanisms leading to these responses are revealed
- Understanding the immediate response of electron fluxes to different solar wind drivers is crucial for forecasting overall belt dynamics
- The phase space density analysis was conducted for electrons at relativistic and ultrarelativistic energies

Corresponding author: M. M. H. Kalliokoski, `milla.kalliokoski@helsinki.fi`

Abstract

Coronal mass ejection driven sheath regions are one of the key drivers of drastic outer radiation belt responses. The response can however be significantly different based on the sheath properties and associated inner magnetospheric wave activity. We performed here two case studies on the effects of sheaths on outer belt electrons of various energies using data from the Van Allen Probes. One sheath caused a major geomagnetic disturbance and the other one had only a minor impact. We especially investigated phase space density of high-energy electrons to determine the dominant energization and loss processes taking place during the events. Both sheaths produced substantial variation in the electron fluxes from tens of kiloelectronvolts up to ultrarelativistic energies. The responses were however almost the opposite: the geoeffective sheath led to enhancement, while the nongeoeffective one caused a depletion throughout most of the outer belt. The case studies highlight that both inward and outward radial transport driven by ultra-low frequency waves, combined with compression of the magnetopause, played an important role in governing electron dynamics during these sheaths. Chorus waves also likely caused a local peak in phase space density, leading to the energization of the ultrarelativistic population during the geoeffective event. The occurrence of chorus waves was based on measurements of precipitating and trapped fluxes by low-altitude Polar Operational Environmental Satellites. The distinct responses and different mechanisms in action during these events are related to differing levels of substorm activity and timing of the peaked solar wind dynamic pressure in the sheaths.

1 Introduction

The outer Van Allen radiation belt in the Earth's inner magnetosphere hosts electrons over a wide range of energies. These electrons experience significant variations over both short and long timescales driven by various acceleration, transport and loss processes. Adiabatic processes can lead to reversible changes in fluxes (the *Dst* effect, see, e.g., Kim & Chan, 1997) when electrons move radially inward or outward conserving all three adiabatic invariants. Irreversible changes occur when the conservation of one or more adiabatic invariants is violated. Different waves in the inner magnetosphere play a key role in such electron dynamics (see Thorne, 2010). For example, electromagnetic ion cyclotron (EMIC) waves scatter relativistic electrons into the loss cone leading to precipitation loss into the upper atmosphere (e.g., Summers & Thorne, 2003; Kurita et al., 2018). Whistler mode chorus waves can also cause precipitation loss but are rather the dominant cause of local acceleration in the heart of the outer radiation belt (e.g., Bortnik & Thorne, 2007; Thorne et al., 2013; Jaynes et al., 2015). Ultra-Low Frequency (ULF) wave driven radial transport can act to energize outer belt electrons (e.g., Su et al., 2015) or contribute to losses at the magnetopause (e.g., Shprits et al., 2006; Turner, Shprits, et al., 2012). Understanding which mechanisms govern the outer belt electron dynamics and response under observed solar wind conditions is important for maintaining safe operation of spacecraft travelling through or residing in the belt. This is especially paramount for the increasingly common nanosatellites whose small size limits the amount of shielding making them more vulnerable to anomalies induced by intense electron fluxes.

The key drivers of magnetospheric disturbances are interplanetary coronal mass ejections (ICMEs), slow-fast stream interaction regions (SIRs) and the following fast wind (e.g., Kilpua, Balogh, et al., 2017). Since these large-scale structures generally have different solar wind conditions, the response of the outer radiation belt electron populations to them varies (e.g., Kataoka & Miyoshi, 2006; Kilpua et al., 2015; Turner et al., 2019). A typical ICME is composed of a leading shock, a sheath region and the ejecta. Similarly, these regions have distinct magnetospheric impact (Kilpua, Koskinen, & Pulkkinen, 2017). Statistical studies of solar wind properties and geomagnetic activity during ICME sheaths indicate that sheaths are associated with elevated interplanetary magnetic field magnitude, solar wind speed, density and dynamic pressure and that their geoeffectiveness depends on the ejecta properties (Yermolaev et al., 2015, 2017, 2018; Lugaz et al., 2016; Masías-Meza et al., 2016; Kilpua et al., 2019; Kalliokoski et al., 2020). Sheaths contain a high level of turbulent fluctuations in the magnetic field (e.g., Moissard et al., 2019). As detailed in previous studies (Kilpua et al., 2013, 2015; Hietala et al., 2014; Kalliokoski et al., 2020), sheaths tend to cause intense wave activity in the inner magnetosphere, in particular EMIC and ULF Pc5 waves, as well as strong compression of the magnetosphere. The response of electron populations in the outer radiation belt can also be different during sheaths and ejecta. In particular, the turbulent and compressed sheaths can cause deep and sustained depletion of MeV electrons (Hietala et al., 2014; Kilpua et al., 2015; Alves et al., 2016; Da Silva et al., 2020; Kalliokoski et al., 2020), but can also lead to their enhancement (Turner et al., 2019). Turner et al. (2019) also found that sheaths tend to cause a two-part outer belt structure at MeV energies.

Many studies of the outer radiation belt response consider events generating moderate or stronger geomagnetic storms (e.g., evaluated with Dst or $SYM\text{-}H$ index dropping below -50 nT; Gonzalez et al., 1994) and assess the changes in electron flux over long time periods, up to a few days, and can even exclude the day of the storm in their quantitative analysis (e.g., O'Brien et al., 2001; Reeves et al., 2003; Turner et al., 2015; Moya et al., 2017). Investigations of the response to sheaths have generally used a similar approach (Kilpua et al., 2015; Turner et al., 2019). It has however been shown that significant variation in the outer belt electron fluxes can occur also during small storms and nonstorm periods (e.g., Schiller et al., 2014; Anderson et al., 2015; Katsavrias et al., 2015). The statistical analysis in Kalliokoski et al. (2020) detailed the immediate (6 h) response of the outer belt electrons to both geoeffective and nongeoeffective sheaths from source to ultrarelativistic energies (10s keV – several MeV). Regardless of whether they cause a geomagnetic storm or not, sheaths predominantly deplete the outer parts ($L > 4$) of the outer belt. Geoeffective sheaths often cause depletion also at lower L-shells at MeV energies. Source and seed populations (10s – 100s keV) are similarly enhanced at $L > 4$ during sheaths, while the geoeffective sheaths also enhance the fluxes at $L < 4$. The study also revealed a clear energy dependence of the depletion. While losses mainly occur at MeV energies, the likelihood of depletion of the seed population (100s keV) increases with radial distance. This was concluded to be likely due to wave-particle interactions dominating the losses in the inner part of the belt, in particular by EMIC waves that can cause rapid loss at MeV energies (e.g., Summers & Thorne, 2003; Kurita et al., 2018), and due to intense substorms effectively replenishing the source and seed populations. Losses at high L-shells were suggested to be dominated by magnetopause shadowing arising from the combination of the magnetopause inward incursion and ULF Pc5 wave driven outward radial transport (e.g., Turner, Shprits, et al., 2012). The determination of the exact physical mechanisms causing the depletion and enhancement during sheaths however needs a more detailed analysis.

Phase space density (PSD), which is obtained by converting electron fluxes from a function of energy and pitch angle into adiabatic invariant coordinates (see, e.g., Green & Kivelson, 2004), provides a useful tool for such analysis. Since PSD remains constant for adiabatic processes, the evolution of the shape of PSD radial profiles can be used to infer the electron acceleration and loss mechanisms in the radiation belts (e.g., Green, 2006; Chen, Reeves, & Friedel, 2007; Turner, Shprits, et al., 2012; Shprits et al., 2017). That is, PSD allows for distinguishing between adiabatic and nonadiabatic effects, as well as between local acceleration and local losses from those caused by radial transport and magnetopause shadowing. A drawback of the method is that calculating the adiabatic invariants requires the use of a global geomagnetic field model. Deviations in the model from the real conditions, especially during storms when the magnetosphere becomes complex, lead to uncertainties in PSD (Chen, Friedel, et al., 2007; Morley et al., 2013; Boyd et al., 2014). Uncertainties are also introduced by errors in the instrument measurements and possible interpolations and fits that need to be done to acquire adequate resolution in PSD (Turner, Angelopoulos, et al., 2012). Nevertheless, careful PSD analysis is advantageous in investigating nonadiabatic outer belt electron dynamics on short timescales, for example, during the sheath and ejecta of an ICME (Da Silva et al., 2020).

Da Silva et al. (2020) studied an ICME sheath region that produced a small geomagnetic storm and a dropout in relativistic electron fluxes. Examining wave measurements and modeling results, they found that the dropout was likely caused by magnetopause shadowing along with ULF wave driven outward radial diffusion and local loss via pitch angle scattering by chorus and EMIC waves, which was confirmed by the PSD analysis. They concluded that wave-particle interactions were efficient only during the sheath, and thus different ICME sub-structures generate a different outer belt response. It is therefore interesting to compare whether similar processes dominate the electron response during other sheaths.

In this paper, we analyze the outer radiation belt electron response to two distinct ICME sheaths. One sheath was geoeffective causing a notable magnetospheric disturbance (min. $SYM\text{-}H$ of -90 nT), while the other was nongeoeffective, i.e., it did not cause a significant geomagnetic storm (min. $SYM\text{-}H$ of -32 nT). This selection of events allows us to compare how the outer belt electron populations are shaped by a geoeffective and a nongeoeffective sheath, both of which can be important for radiation belt electron dynamics but which have significant differences in their responses, as indicated by Kalliokoski et al. (2020). Similar to earlier studies (e.g., Hietala et al., 2014; Kilpua et al., 2015, 2019; Kalliokoski et al., 2020), this work highlights that significant variations occur in the outer belt electron fluxes during ICME-driven sheath regions. We further show that such drastic changes can also arise at ultrarelativistic energies, and even during a nongeoeffective sheath. Such relatively short time-scale variations ($\sim$ half-a-day) are missed by studies considering the electron response over the whole geomagnetic storm period that often lasts over several days. In contrast to the prior sheath studies, we perform here a detailed analysis of electron phase space density, which combined with consideration of the inner magnetospheric wave activity, sheds light on the dominant mechanisms that act on the outer belt electrons. We focus on the nonadiabatic dynamics driven specifically by the sheath region impact, and our aim is to compare and contrast how the outer radiation belt responds to sheaths with different properties. The various data and methodology used in this study are presented in Section 2. In Section 3, we describe the observations of the properties of the two sheaths, as well as the activity of waves and the outer belt conditions in terms of both electron flux and PSD during the sheath events. We discuss the results and especially the interpretation of the PSD radial profiles in Section 4 and conclude in Section 5.

2 Data and Methods

2.1 Solar Wind Data

We consider two interplanetary coronal mass ejections (ICMEs) with sheath regions, one on 2 October 2013 and the other on 15 February 2014. The timing of the sheath regions were based on the shock times from the University of Helsinki Heliospheric Shock Database (`http://www.ipshocks.fi`, last access: 4 June 2021) and visual inspection of the solar wind data to determine the ejecta interval. The characteristics of sheath regions and ejecta and the determination of their boundaries are discussed, for example, in Richardson and Cane (2010) and Kilpua, Koskinen, and Pulkkinen (2017). Both events are listed as magnetic clouds in the Richardson and Cane ICME list (`http://www.srl.caltech.edu/ACE/ASC/DATA/level3/icmetable2.htm`, last access: 4 June 2021), i.e., the ejecta have signatures of a magnetic flux rope.

We used solar wind data measured by the Wind spacecraft (Lepping et al., 1995; Ogilvie et al., 1995), and geomagnetic activity indices (AL and $SYM\text{-}H$) were taken from the OMNI database. Both Wind and OMNI data had 1 min resolution. Wind and OMNI data were obtained via the NASA Goddard Space Flight Center (NASA–GSFC) Coordinated Data Analysis Web (CDAWeb, `https://cdaweb.gsfc.nasa.gov/index.html/`, last access: 4 June 2021). The Wind data were propagated to the bow shock nose. We used the Wind data instead of solar wind properties from OMNI database since the latter had data gaps during the periods of interest.

The solar wind data is also used to calculate the subsolar magnetopause location with the Shue et al. (1998) model.

2.2 Wave Activity and Chorus Proxy

Ultra-low frequency (ULF) waves in the Pc5 and electromagnetic ion cyclotron (EMIC) ranges were obtained from a Geostationary Operational Environmental Satellite (GOES-15) at $L \sim 6.6$. The magnetic field data has a time resolution of 0.512 s (Singer et al., 1996). We derived the ULF power spectrum via wavelet analysis of the magnetic field magnitude measured by GOES-15, and calculated the mean over the frequency range 2–7 mHz for Pc5 pulsations and 0.1–1 Hz for EMIC waves (Jacobs et al., 1964), where the upper bound for EMIC waves is restricted by the GOES time resolution. We note that ULF wave activity at the Van Allen Probes location might not always be represented by the ULF observations at geostationary orbit (Engebretson et al., 2018; Georgiou et al., 2018).

Data of very low frequency (VLF) wave activity, namely whistler mode chorus and plasmaspheric hiss, were obtained from the Electric and Magnetic Field Instrument Suite and Integrated Science (EMFISIS; Kletzing et al., 2013) on the Van Allen Probes. Specifically, we used the level-2 waveform receiver diagonal spectral matrix data that has a frequency range from 2 Hz to 12 kHz and 6 s time cadence available on the EMFISIS webpage (`https://emfisis.physics.uiowa.edu/data/index`, last access: 4 June 2021). Lower band chorus has the frequency range 0.1–0.5 f_{ce} and upper band chorus has 0.5–0.8 f_{ce} (Burtis & Helliwell, 1969; Koons & Roeder, 1990), where f_{ce} is the electron cyclotron frequency, which was here obtained from the Tsyganenko and Sitnov (2005) geomagnetic field model. Chorus waves occur outside the dense plasmasphere, whereas plasmaspheric hiss occurs inside the plasmasphere at frequencies from 100 Hz to 0.1 f_{ce}. To discriminate chorus from plasmaspheric hiss, we estimated the plasmapause location based on the electron density derived from the upper hybrid resonance frequency (Kurth et al., 2015). The density is provided as a level-4 data product by the EMFISIS team.

Van Allen Probes measure the local chorus wave activity and can therefore miss the global chorus distribution. This is especially the case when the perigee of the spacecraft is in the dawn sector because chorus predominantly occurs at $L > 4$ on the dawnside (e.g., Lam et al., 2010). In both considered events, little local chorus activity was observed by Van Allen Probes. The perigee of both spacecraft was at dawn for the 2 October 2013 event and at midnight for the 15 February 2014 event, indicating that their observations might not reflect the global chorus activity. Thus, we used low-energy electron precipitation data as a proxy for chorus activity (Chen et al., 2014).

Electron precipitation data is provided by the low-altitude and polar-orbiting Polar Operational Environmental Satellites (POES). We used data from the Medium Energy Proton and Electron Detector (MEPED) instrument of the Space Environment Monitor (SEM-2; Evans & Greer, 2004) suite on board six such polar-orbiting spacecraft (NOAA-15, NOAA-16, NOAA-18, NOAA-19, MetOp-A and MetOp-B). MEPED measures electrons with two detectors, namely the 0° and 90° telescopes. The former points radially away from the Earth, primarily along the local magnetic field and loss cone, while the latter is antiparallel to satellite velocity, i.e. perpendicular to the 0° telescope viewing direction, and primarily measures trapped fluxes. The electron channels measure at energies > 30 keV, > 100 keV and > 300 keV. The MEPED data used here has been reprocessed (Asikainen & Mursula, 2013; Asikainen, 2017) to correct for proton contamination and other instrumental problems that affect the POES measurements (see, e.g., Rodger et al., 2013).

At high latitudes, the MEPED 0° telescope underestimates precipitating fluxes as the bounce loss cone is significantly larger than the 30° field of view of the detector (Rodger et al., 2013). On the other hand, the 90° telescope measures some fluxes in the loss cone at high latitudes in addition to the trapped flux (Rodger et al., 2010). Therefore, to better estimate the precipitating fluxes at high latitudes, which were considered in this study, we combined the data from the two detectors and considered the geometric mean of the fluxes (e.g., Hargreaves et al., 2010; Rodger et al., 2013; George et al., 2020):

$$j_{precip} = \sqrt{j_0 * j_{90}}, \tag{1}$$

where j_0 and j_{90} are the fluxes from the 0° and 90° telescopes, respectively. We note that by including the 90° telescope measurements we overestimate precipitating flux when trapped fluxes are high, and we might also underestimate precipitation when precipitating fluxes are high during low levels of trapped flux. Nevertheless, in this study where we are considering precipitation qualitatively, we expect this method to provide a better estimate of the precipitating fluxes than the 0° telescope measurements alone.

We used the chorus proxy derived by Chen et al. (2014) which gives the chorus wave power as

$$B_w^2(L) = \frac{j_{precip}(L)}{P * [(L-3)^2 + 0.03]}, \tag{2}$$

where P is a scaling factor. The proxy is restricted to $L > 3.5$. The Van Allen Probes detected almost no chorus waves, so we did not scale the proxy with spacecraft chorus observations and set $P = 1$ which suffices for our qualitative analysis of the chorus activity.

Following Chen et al. (2014) we calculated the chorus proxy for low-energy, 30–100 keV electrons. That is, we subtracted the POES $>$ 100 keV electron channel measurements from the $>$ 30 keV measurements for each detector and combined the data using Eq. 1. The data was then binned 0.1 in L-shell and 100 min in time, which corresponds to the orbital period of POES spacecraft. The high resolution data from multiple spacecraft on polar orbits allows us to inspect the chorus proxy up to high L-shells, and here we show the proxy up to $L = 10$.

2.3 Electron Flux Data and Outer Belt Response Parameter

Outer radiation belt electron fluxes were obtained from the Energetic Particle, Composition, and Thermal Plasma instrument suite (ECT; Spence et al., 2013) on board the twin Van Allen Probes, which provide a wide coverage in electron energy at radial distances up to $L = 6$ (Mauk et al., 2013). The Magnetic Electron Ion Spectrometer (MagEIS; Blake et al., 2013) observes the source, seed and core electron populations from 30 keV to 1.5 MeV, while the Relativistic Electron Proton Telescope (REPT; Baker, Kanekal, Hoxie, Batiste, et al., 2013) measures the core and ultrarelativistic populations from 1.8 to 10 MeV. The employed MagEIS fluxes were background corrected when available (Claudepierre et al., 2015). The L-shell of the spacecraft, derived from the Tsyganenko and Sitnov (2005) geomagnetic field model, was acquired from the magnetic ephemeris data available on the ECT website (`https://rbsp-ect.lanl.gov/`, last access: 4 June 2021).

We determined the outer radiation belt response to the sheath region, following Kalliokoski et al. (2020), by calculating the response parameter (R) as the ratio of the post-sheath flux average to the pre-sheath flux average. The flux average was taken over 6 h. The response parameter was computed for 0.1 sized L-shell bins in $L = 2$–6 using the level-2 spin-averaged differential electron flux data from both Van Allen Probes. We calculated the response parameter for four energy channels representing the source (54 keV), seed (346 keV), core (1064 keV) and ultrarelativistic (4.2 MeV) populations. The response is categorized as *depletion* when the flux average decreased by over a factor of 2 ($R < 0.5$), *enhancement* when the flux average increased by over a factor of 2 ($R > 2$) and *no change* when the flux average remained on a similar level ($0.5 \leq R \leq 2$). Note that in the visualization of the electron fluxes we have chosen 4 h time bins (instead of 6 h) for a clearer and more detailed view of the temporal evolution.

The method of computing the response parameter is adapted from Reeves et al. (2003) and Turner et al. (2015, 2019), who applied it to study the outer belt response to entire geomagnetic storms and considered periods ranging from 12 h up to a few days. In contrast, we focus here on the immediate response of the electron fluxes due to the sheath region, which we aim to capture with the 6 h averaging period. The post-sheath flux average is embedded in the ejecta, but we expect the main response due to the ejecta to occur at later times. We do note that the ejecta in both studied events were shorter than the sheath regions. The ejecta duration is 15.0 h on the 2 October 2013 event and 8.6 h on the 15 February 2014 event – the latter is close to the averaging period but we see that the main changes in electron fluxes occur during the sheath region. The ejecta times match approximately with those reported in the Richardson and Cane ICME list.

2.4 Phase Space Density (PSD) Analysis

For a more detailed investigation of the acceleration, transport and loss processes taking place during the events, we calculated the phase space density (PSD) at chosen adiabatic invariant coordinates (e.g., Green & Kivelson, 2001, 2004; Green, 2006; Chen et al., 2005; Chen, Reeves, & Friedel, 2007; Turner, Shprits, et al., 2012; Turner, Angelopoulos, Li, et al., 2014; Shprits et al., 2017). Adiabatic invariants correspond to the three constants of motion in the geomagnetic field when changes occur slowly (e.g., Roederer, 1970): gyration about field lines (1st invariant, μ), bounce along field lines (2nd invariant, K) and drift about the Earth (3rd invariant, L^*).

We used the level-3 pitch angle resolved electron fluxes from MagEIS and REPT on both Van Allen Probes to compute the PSD. The size of the pitch angle bins is 16.4° for MagEIS and 10.6° for REPT. We acquired invariants K and L^* from the ECT magnetic ephemeris files that are computed with the global magnetic field model of Tsyganenko and Sitnov (2005) (TS04D; `https://rbsp-ect.lanl.gov/`, last access: 4 June 2021). The time resolution of these modeled parameters is typically 5 min and the pitch angle resolution is 5°. K and L^* were interpolated to the equatorial pitch angles, mapped from the Van Allen Probes' local pitch angle measurements using the TS04D modeled equatorial magnetic field magnitude. The magnetic moment μ was calculated using the magnetic field magnitude observed by Van Allen Probes' magnetometers (EMFISIS; Kletzing et al., 2013) and the local pitch angle measurements. The electron fluxes were binned to 1 min prior to calculating PSD.

We used all low and medium energy channels from MagEIS, except the highest medium channel which was replaced by the first MagEIS high channel. The employed MagEIS channels cover the energy range from 30 keV to 1 MeV, while we use REPT to capture the ultrarelativistic electrons from 1.8 MeV to 9.9 MeV. In order to improve the energy resolution for the PSD calculation, we added two artificial energy channels in between each instrument channel. Fluxes in these added channels were interpolated from the measured fluxes. The central energies of the artificial channels were defined as the geometric mean of the lower and upper limits as defined in Chen et al. (2005). We also followed the Chen et al. (2005) formulation in calculating the relativistic momenta for each channel and converting electron fluxes to PSD. The steps in the calculation of PSD at fixed μ and K are summarized in, e.g., Hartley and Denton (2014). We note that no fitting of the energy or pitch angle distributions were performed in our method.

We investigated electrons mirroring near the equator by fixing K to an upper limit of 0.05 $R_E\mathrm{G}^{1/2}$. Two energy ranges were evaluated, $\mu = (300 \pm 10)$ MeV/G and $\mu = (3000 \pm 100)$ MeV/G, in order to probe the core and ultrarelativistic electron populations. The PSD of the core and ultrarelativistic populations were calculated using MagEIS and REPT data, respectively. The PSD values were binned to $\Delta L^* = 0.15$ when plotting the L^* profile, as multiple values of PSD can be found at similar L^*. The purpose of the binning is to smooth the profiles and indicate the average shape of the curves. We have provided the unbinned PSD profiles in the Supporting Information (Figure S2).

The fluctuation in PSD at similar L^* arises from the employed ranges in μ and K. The ranges are broad enough for PSD points with μ and K values within these ranges to be found at two or more energy channels or pitch angle bins at the same time. The different bins correspond to different values of PSD, but have similar L^*, causing the fluctuations. Fluctuations seem to arise in particular from large jumps (∼order of magnitude) in flux between REPT energy channels. Similar fluctuation effects are seen in other PSD studies using ranges (e.g., Schiller et al., 2014). Naturally, the fluctuations increase for larger ranges of μ and K. The additional interpolated energy channels, while increasing the energy resolution, reproduce the fluctuations originating from flux variation between the instrumental channels. On the other hand, these ranges allow for a better resolution in PSD as opposed to fixing μ and K to a single value. We have chosen the ranges for this study as a compromise of being restrictive enough to remove major fluctuations, but broad enough to allow for a sufficient resolution of PSD points as a function of L^*.

3 Results

In this section, we present the geospace response to two ICME events with sheath regions on 2 October 2013 and 15 February 2014 in terms of solar wind parameters, geomagnetic activity indices, inner magnetospheric wave activity, outer radiation belt electron fluxes and phase space density.

3.1 Overview of Solar Wind Observations

Figure 1 shows the evolution of solar wind parameters and geomagnetic activity during the two analyzed events, 2 October 2012 (Event 1) on the left and 15 February 2014 (Event 2) on the right. The panels give from top to bottom the magnetic field magnitude, magnetic field components in Geocentric Solar Magnetospheric (GSM) coordinate system, solar wind speed, solar wind dynamic pressure, subsolar magnetopause position from the Shue et al. (1998) model, and *AL* and *SYM-H* indices. The sheath is depicted with the blue shaded area.

For Event 1, the shock associated with the sheath region occurred on 2 October 2013 at 1:11 UT (or at 1:58 UT when time-shifted to the magnetopause). The sheath extended until 23:50 UT on the same day (0:37 UT on the next day at magnetopause), spanning 22.7 h. The interplanetary magnetic field (IMF) direction had large-amplitude fluctuations and the IMF magnitude and dynamic pressure were enhanced during the front part of the sheath region, which was concurrent with the largest geomagnetic impact, as shown by both the *SYM-H* and *AL* indices. The sheath caused a moderate geomagnetic storm with a minimum *SYM-H* of −90 nT reached shortly after the shock impact. The IMF Bz-component changed from strongly negative to positive after a few hours in the sheath and turned slightly negative near the end of the sheath causing some substorm activity. The ejecta did not cause a geomagnetic storm or any substorm activity as the Bz-component was positive during the ejecta. The subsolar magnetopause was compressed beyond 10 Earth radii and briefly beyond the geostationary orbit during the front part of the sheath region. After reaching the minimum value, the magnetopause gradually relaxed to a nominal position during the rest of the sheath and moved to large distances ($\sim 15\ R_E$) during the low dynamic pressure ejecta.

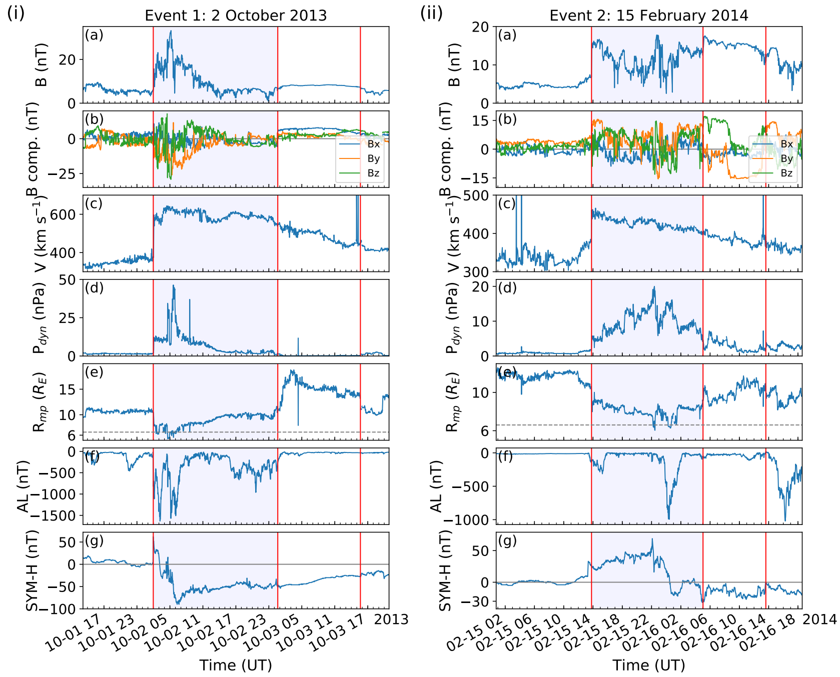

Figure 1. Solar wind properties and geomagnetic activity indices for the sheath events (i) on 2 Oct 2013 and (ii) on 15 Feb 2014. (a) Magnetic field magnitude, (b) magnetic field components in the geocentric solar magnetospheric coordinate system, (c) solar wind speed, (d) solar wind dynamic pressure, (e) subsolar magnetopause location from the Shue et al. (1998) model with the location of the geostationary orbit indicated (6.6 R_E), (f) *AL* index and (g) *SYM-H* index. The red vertical lines indicate the shock, ICME ejecta leading edge and ejecta trailing edge in UT (universal time). The shaded area marks the sheath interval. The Wind data has been shifted from L1 to the magnetopause.

The shock of Event 2 was observed on 15 February 2014 at 12:46 UT (13:47 UT at magnetopause) and the sheath lasted until 16 February at 4:00 UT (5:01 UT at magnetopause), i.e. the sheath duration was 15.2 h. The IMF direction presented again large-amplitude fluctuations during the sheath, but now the largest fluctuations with southward fields occurred in the trailing part of the sheath. In the front part of the sheath, the IMF was directed northward. Dynamic pressure was elevated and peaked at the centre of the sheath, and consequently, the magnetopause reached closest to Earth in the middle of the sheath. Again, the magnetopause was briefly pushed beyond geostationary orbit. The magnetopause then relaxed back to its nominal position during the ejecta. There was some substorm activity during the sheath, as evidenced by the *AL* index. A small substorm occurred just after the shock passage, while a bigger took place close to the sheath trailing edge. The *SYM-H* index was first positive during most of the sheath and then decreased to minimum value of −32 nT at the very end of the sheath. The *SYM-H* index remained negative but above −30 nT during the ejecta.

The main difference between the two events was the strength of the geomagnetic storm, as evidenced by the *SYM-H* index, and the location of the strong substorm activity, seen in the *AL* index, which coincided with the *SYM-H* minimum. Stronger geomagnetic activity occurred near the start of the sheath with a −90 nT *SYM-H* minimum for the geoeffective Event 1. On the contrary, for the nongeoeffective Event 2, which

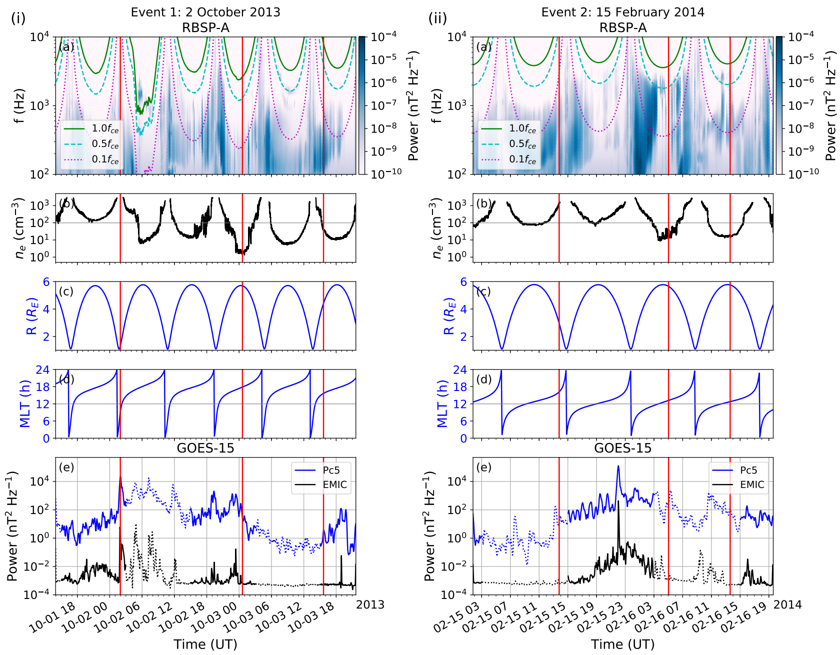

Figure 2. Very-low and ultra-low frequency (VLF and ULF) wave activity (i) on 2 Oct 2013 and (ii) on 15 Feb 2014. (a) Power spectrum of VLF waves from the EMFISIS instrument on Van Allen Probe A. The curves indicate different values of the equatorial gyrofrequency f_{ce} calculated from the TS04D geomagnetic field model. Chorus waves have frequencies $> \quad 0.1 f_{ce}$ outside the plasmasphere, and plasmaspheric hiss is present at lower frequencies. (b) Estimated electron density, where the horizontal line at 100 cm^{-3} illustrates an estimate of the plasmapause location. (c) TS04D model spacecraft radial location and (d) magnetic local time (MLT). (e) Wave power of ULF Pc5 and EMIC waves calculated with wavelet analysis from the magnitude of the magnetic field as measured by GOES-15. Solid and dotted lines indicate when the GOES spacecraft was on the dayside and nightside, respectively. The red vertical lines indicate the sheath and ICME ejecta intervals.

had a *SYM-H* minimum of −32 nT, the stronger subtorm activity occurred near the end of the sheath.

3.2 Inner Magnetospheric Wave Activity

The wave activity in the inner magnetosphere is shown in Figure 2. Again the left panels show the data for Event 1 and the right panels for Event 2. The panels give from top to bottom the power spectrum of chorus and hiss waves; plasma density; location of the spacecraft; magnetic local time (MLT); and the ULF Pc5 and EMIC wave powers. The power spectrum plot includes the f_{ce}, $0.5 f_{ce}$ and $0.1 f_{ce}$ curves of equatorial gyrofrequency represented by the green, cyan and magenta curves. We show here data for Van Allen Probe A and GOES-15 only, the similar plot for Van Allen Probe B and GOES-13 is found in the Supporting Information (Figure S1).

Van Allen Probes are expected to be inside the plasmasphere when the density is high. Here we have marked 100 cm^{-3} as the limiting value (e.g., Malaspina et al., 2018) with the horizontal line in panels b.

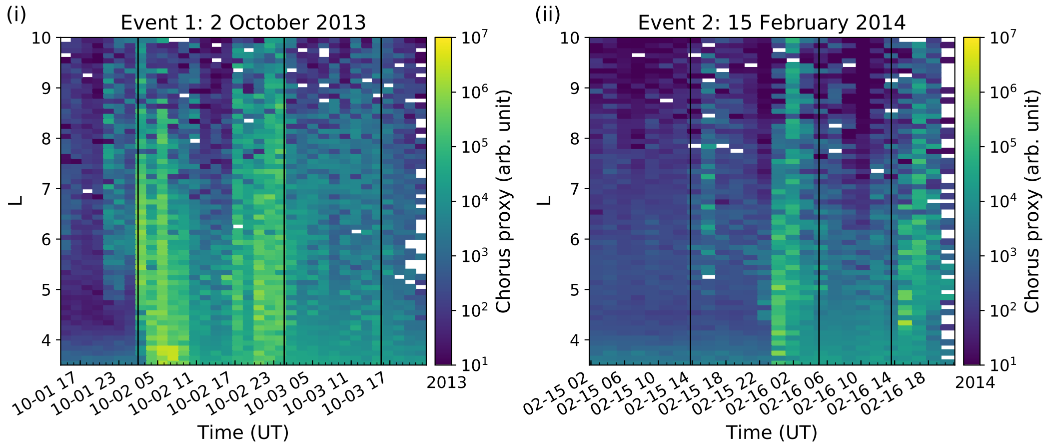

Figure 3. Chen et al. (2014) chorus proxy (with scaling factor $P = 1$) calculated from the geometric mean of the low-energy (30–100 keV) POES precipitating and trapped electron fluxes (i) for 2 Oct 2013 and (ii) for 15 Feb 2014.

The top panel of Figure 2 shows that, according to the Van Allen Probes measurements during the sheath of Event 1, there was only little chorus activity, but hiss was present almost throughout the whole sheath. This was also the case for Event 2. For Event 1, during the period ∼12–18 UT on 2 October, Van Allen Probe B was inside the plasmasphere according to density (see Figure S1), so the stripes of enhanced emission extending to $> 0.1 f_{ce}$ are likely plasmaspheric hiss. At this time Van Allen Probe A was mostly outside the plasmasphere according to the density, and saw only weak enhancements in the lower chorus range. The same applies to emission detected at $> 0.1 f_{ce}$ for Event 2 when density was close to the 100 cm^{-3} limit.

The ULF Pc5 and EMIC wave power were in turn elevated for Event 1 during the sheath region, and especially so in the front part of the sheath. The EMIC power was low during most of the trailing part of the sheath and remained low during the ejecta, while the ULF Pc5 remained elevated and then quickly dropped during the ejecta. Event 2 also showed considerably elevated Pc5 and EMIC power throughout the sheath, but the highest power occurred at the centre of the sheath when the dynamic pressure peaked. Similar results were measured by GOES-13 (see Figure S1).

For both events we see (panels d in Figure 2) that Van Allen Probes spent only a relatively short time on the dawnside, i.e. between 0 and 12 UT, where the main chorus activity is expected to occur. To obtain a better estimate of the chorus activity we investigated the chorus proxy based on Chen et al. (2014) and POES 30 to 100 keV electrons (see Section 2.2). These are shown in Figure 3 for both of our events.

The left panel of Figure 3 reveals that in Event 1 significant chorus wave activity was expected to occur in particular close to the shock and ejecta leading edges where the substorms occurred. According to the proxy, the chorus activity extended throughout the outer belt, from $L = 3.5$ to about $L = 9$, and peaked at $L = 3.5$–4 just after the shock, i.e. when the strongest substorm took place and *SYM-H* dipped. For Event 2, there was one interval of intense chorus close to the ejecta leading edge, again coinciding with the strongest substorm.

To summarize, both events caused significant Pc5 and EMIC activity, although wave activity peaked in different parts of the sheath region. The chorus activity was largely missed by the Van Allen Probes due to their orbit missing most of the dawnside, but the

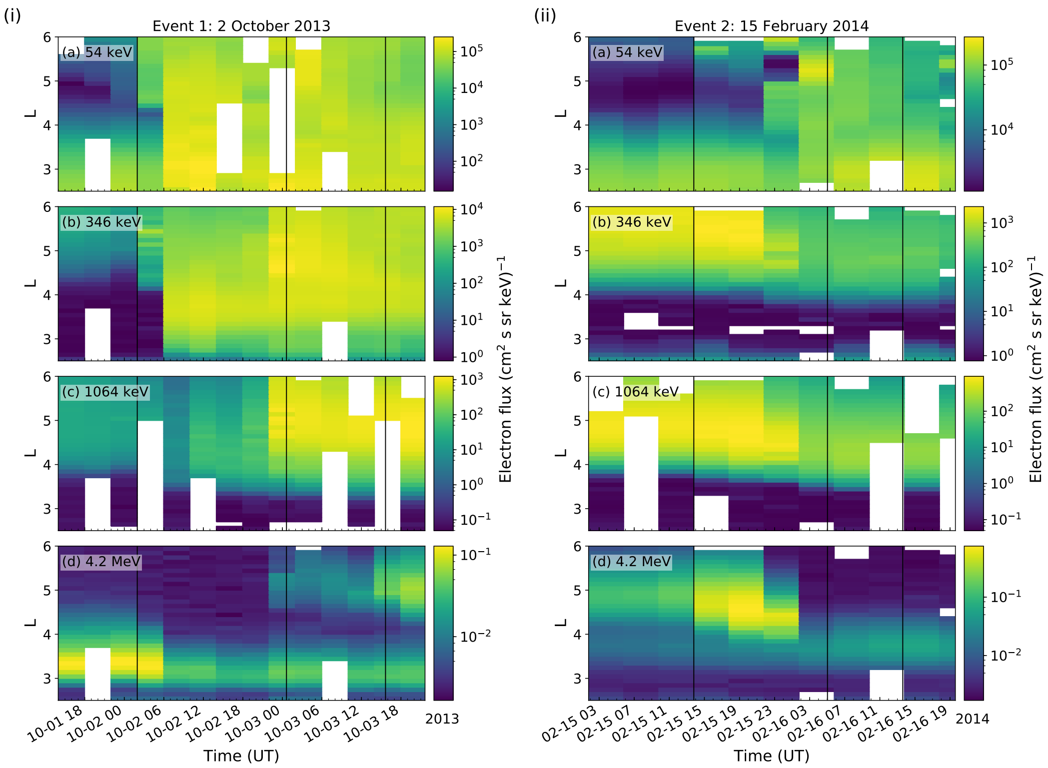

Figure 4. The spin-averaged electron fluxes measured by MagEIS at (a) 54 keV, (b) 346 keV and (c) 1064 keV and (d) by REPT at 4.2 MeV for the sheath events (i) on 2 Oct 2013 and (ii) on 15 Feb 2014. The data are combined from both Van Allen Probes and are binned by 4 hours in time and 0.1 in L-shell. The MagEIS electron fluxes are background corrected, except for the 54 keV fluxes in Event 2. The vertical lines mark the sheath region and ICME ejecta intervals.

chorus proxy suggested that the more geoeffective Event 1 had in particular significant chorus wave activity. The chorus activity was less intense and hiss more intense in Event 2. These indicate the first event to be more conductive to produce enhancement of core electrons, while the second is more susceptible to prolonged depletion.

3.3 Electron Flux Observations

Electron fluxes from four Van Allen Probes energy channels representing the source, seed, core and ultrarelativistic populations are presented in Figure 4.

For Event 1, source and seed electrons were enhanced near the start of the sheath during the strong substorm activity. Source and seed electron fluxes increased throughout the outer belt, but the strongest enhancement took place at $L = 3$–4. This is consistent with the chorus proxy in Figure 3 showing the peak at similar L range. Near the end of the sheath, during moderate substorm activity, the seed fluxes were further enhanced at $L > 4$. For Event 2, the background corrected electron flux data at source energies is not available, so we have shown the uncorrected fluxes instead. Contamination is not significant in this energy channel, so use of the uncorrected flux data has minimal impact on the analysis. For Event 2, fluxes increased at source energies near the end of the sheath. Seed electrons were lightly enhanced at the shock, depleted near the end part of the sheath and remained at about that depleted level during the ejecta. This is consistent with much weaker substorm activity during Event 2.

On the other hand, for Event 1 core and ultrarelativistic fluxes decreased soon after the start of the sheath. Depletion was more dramatic for the highest energy and occurred in two parts, first a stronger decrease on 2 October at ∼6 UT followed by a further depletion a bit later at ∼14 UT. A weak remnant belt however remained from the high pre-event fluxes at $L \sim 3$. Both the core and ultrarelativistic populations enhanced at $L > 4$ near the end of the sheath, similar to lower energies. For the highest energies, the remnant belt also intensified simultaneously, causing a clear two-part structure of the outer belt (Baker, Kanekal, Hoxie, Henderson, et al., 2013; Pinto et al., 2018).

For Event 2, similar to seed electrons, core electrons had a small enhancement at the shock. Ultrarelativistic electrons in turn experienced relatively strong enhancement at higher L-shells, with about an order of magnitude increase throughout $L > 4$. The band of the enhanced fluxes at MeV energies narrowed and moved to lower L-shells, and then depleted during the end part of the sheath simultaneously with the seed electrons. Again, no further significant changes were observed during the ejecta. For Event 2 the outer belt had a two-part structure at ultrarelativistic energies before the shock arrival that was destroyed during the sheath as the depleted fluxes at outer L-shells were not replenished, contrary to Event 1.

The overall response is given in Figure 5 in terms of the response parameter (Section 2.3) as a function of L-shell for the same four energy channels. This picture emphasises the immediate response to the sheath. Firstly, the figure highlights that for the geoeffective event (Event 1) the sheath enhanced fluxes from source to core energies at all L-shells investigated (i.e. values above the red dashed line), while for ultrarelativistic energies fluxes enhanced only at $L > 5$ and slightly at $L < 3$. For the nongeoeffective event (Event 2), in turn, fluxes mostly stayed unchanged or depleted, apart from source electrons which enhanced at $L > 4$. At other energies, enhancements occurred only at a narrow L range between 3.5–4, with the largest enhancement occurring for core electrons. The deepest depletion occurred for ultra-relativistic electrons at $L > 4$ (i.e., contrary to the geoeffective event for which the fluxes enhanced at this part of the belt). We emphasize that the response parameter neglects the flux dynamics during the sheath, i.e., it only looks at the result after the sheath relative to conditions before the sheath.

3.4 PSD Analysis Results

To gain more insight into acceleration and loss mechanisms during the investigated sheaths, we examined the electron observations using PSD. The results are shown in Figure 6 for Event 1 and Event 2 in the left and right hand panels, respectively. Two different values of magnetic moment μ are considered, $\mu = (300 \pm 10)$ MeV/G and $\mu = (3000 \pm 100)$ MeV/G. The energy corresponding to a certain μ value varies according to geomagnetic field magnitude and thus with L^*. At $L^* = 4$, $\mu = 300$ MeV/G corresponds roughly to 900 keV, i.e. core energies, and $\mu = 3000$ MeV/G corresponds roughly to 3.7 MeV, i.e. ultra-relativistic energies. Squares and dots show the inbound orbits for Van Allen Probes A and B, respectively, and pluses and stars show the outbound orbits. The color coding from purple to yellow indicates the increasing time. Videos highlighting the time evolution of PSD from pass to pass are available in the Supporting Information.

In agreement with electron fluxes discussed in the previous section, for Event 1 and for $\mu = 300$ MeV/G, PSD enhanced at $L^* > 3$. This indicated a combination of inward radial diffusion and substorm injections transported radially inward, and an increasing source population at higher L^*. PSD increased about three orders of magnitude below $L^* = 4$ and about two orders of magnitude at higher L^* in about one full orbit (9 h, from purple to magenta curves). PSD then continued to increase by almost an order of magnitude at $L^* > 4$ during about 12 hours (magenta to orange curves). This enhance-

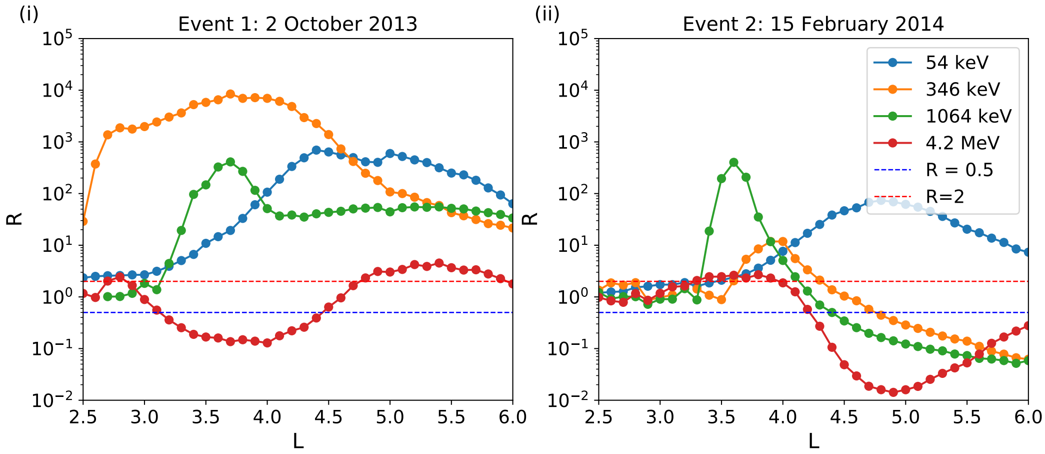

Figure 5. The response parameter (R) as a function of L-shell at four different energies representing the source (54 keV), seed (346 keV), core (1064 keV) and ultrarelativistic (4.2 MeV) populations for the sheath events (i) on 2 Oct 2013 and (ii) on 15 Feb 2014. The response parameter is defined as the ratio of electron flux averaged over 6 hours after and before the sheath region. The blue and red dashed lines show $R = 0.5$ and $R = 2$, respectively, indicating depletion ($R < 0.5$), no change ($0.5 \leq R \leq 2$) and enhancement ($R > 2$) of electron fluxes due to the sheath region.

ment persisted for the duration of the sheath, after which the PSD slightly declined during the ejecta at $L^* > 4$ (orange to yellow curves).

On the other hand, in the front part of the sheath PSD for $\mu = 3000$ MeV/G electrons in Event 1 showed a decrease in PSD at $L^* > 3$, while the PSD increased at $L^* < 3$. This is a typical PSD signature of magnetopause shadowing losses due to combined magnetopause incursion and outward diffusion at higher L^*, and inward diffusion at lower L^* (e.g., Turner & Ukhorskiy, 2020). Later in the sheath and ejecta, PSD at $\mu = 3000$ MeV/G increased considerably at around $L^* \sim 4$–5 and developed a peak. The peak was first detected by Van Allen Probe A during its inbound pass starting at 15:25 UT on 2 October (magenta squares). PSD had increased by an order of magnitude compared to the earlier outbound pass. In the following inbound pass of Van Allen Probe A, starting at 00:10 UT on 3 October, the peak had increased by two orders of magnitude. That is, the peak grew three orders of magnitude in about 12 hours. The outbound pass of Van Allen Probe A between the peak growth observations of the inbound passes did not have PSD available at the considered μ and K ranges. Similarly, PSD was not available from Van Allen Probe B at the time of peak formation and growth, so we cannot confirm the local growing peak with a two-point measurement.

Nevertheless, we calculated the peak growth rate based on the Van Allen Probe A passes before, during and after peak growth (magenta pluses, magenta squares and orange squares, respectively). We considered the three points at $L^* = 4.4$–4.8 at the peak location, and fitted a line to the logarithmic PSD values as a function of time for each of these L^* bins. The mean peak growth rate is 6.3 days^{-1} (i.e., orders of magnitude per day). The formation of this peak is discussed in detail in Section 4. After the peak growth observed by Van Allen Probe A, the peak was sustained at a similar level throughout the ejecta. The location of the peak also slowly drifted to higher L^*, from about $L^* =$ 4.6 to 5, indicating outward radial transport.

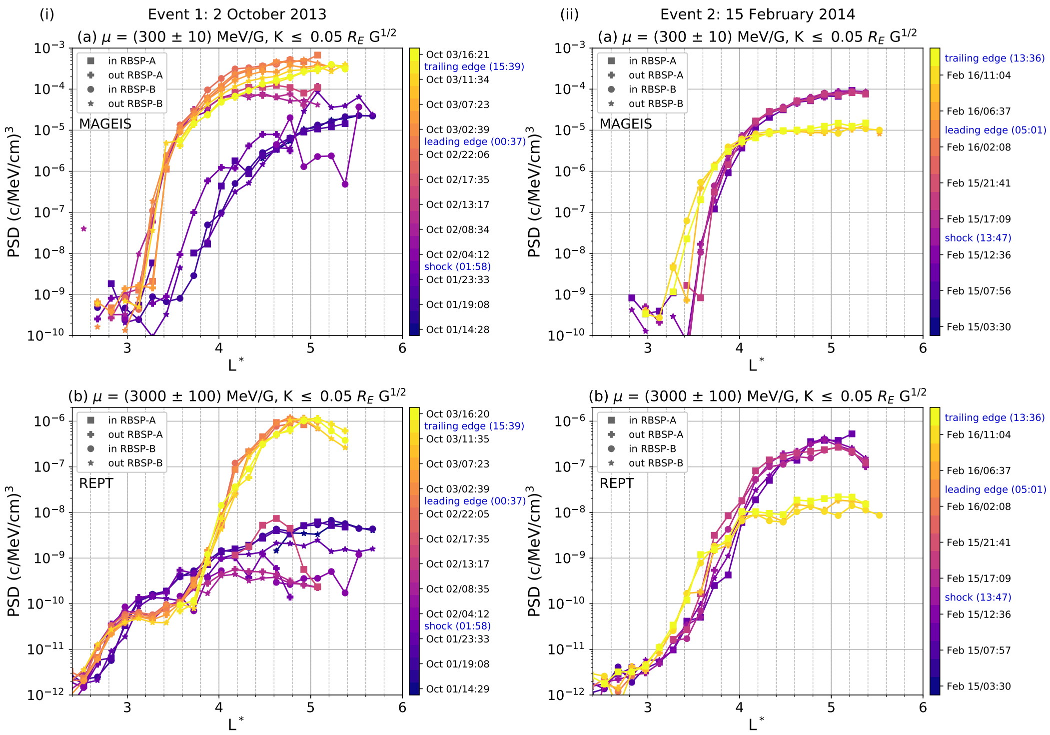

Figure 6. Phase space density (PSD) profiles (i) on 2 Oct 2013 and (ii) on 15 Feb 2014 representing nearly equatorially mirroring electrons with $K \leq 0.05\ R_E\mathrm{G}^{1/2}$. PSD versus L^* is shown for (a) lower energy particles ($\sim$ 900 keV at $L^* = 4$) at $\mu = (300 \pm 10)$ MeV/G and (b) higher energy particles ($\sim$ 3.7 MeV at $L^* = 4$) at $\mu = (3000 \pm 100)$ MeV/G. The profiles have been smoothed by averaging PSD to 0.15 L^* bins per pass. PSD calculations employed the TS04D magnetic field model and Van Allen Probes magnetic field measurements. The satellite passes are color-coded and the corresponding times are indicated in the color bar. The inbound and outbound passes of RBSP-A and RBSP-B are shown with different markers as indicated in the legend.

Onward from the pass starting at 08:35 UT on 2 October, there appeared to be a dip in PSD at $L^* \sim 3.3$ which remained throughout the rest of the event, consistent with Figure 5 (red curve for 4.2 MeV electrons). A local dip is a signature of local loss, mostly likely by EMIC waves (e.g., Aseev et al., 2017; Shprits et al., 2017).

For Event 2, PSD decreased about one order of magnitude at $L^* > 4$ in 13 hours for $\mu = 300$ MeV/G electrons, evidencing magnetopause shadowing and outward diffusion. The PSD profile also shows an increase at $L^* < 4$ caused by inward radial diffusion, which is further evidence for magnetopause shadowing causing the electron dropout, as discussed above for Event 1. It is however unclear if the dropout in PSD at $L^* > 4$ is abrupt or gradual as no PSD data could be derived there at the chosen adiabatic invariant coordinates from 21:41 UT on 15 February to 08:43 UT on 16 February (i.e., the latter half of the sheath region where the dropout in electron fluxes is observed).

Similar PSD evolution took place for $\mu = 3000$ MeV/G electrons in Event 2. There was about one order of magnitude decrease in PSD at $L^* > 4$ in 13 hours. PSD data is missing for the same time period as for $\mu = 300$ MeV/G during the latter part of the sheath, indicating that the spacecraft were not measuring electrons in the chosen K range during this period. Similarly to $\mu = 300$ MeV/G profiles, PSD increased at $L^* < 4$. Therefore, PSD signatures indicate again magnetopause shadowing losses due to combined magnetopause incursion and outward transport. At $\mu = 3000$ MeV/G, the inward radial diffusion was also already observed early in the sheath accompanied by decreasing PSD at the highest probed L^*, as opposed to PSD at $\mu = 300$ MeV/G where increase at $L^* < 4$ was only observed during the ejecta. This indicates that magnetopause shadowing occurred throughout Event 2.

4 Discussion

The overall outer belt electron response, as shown by the response parameter (Figure 5), indicates opposite trends for the two investigated sheath regions. The geoeffective sheath caused a strong enhancement at all energies throughout the outer belt, except at $L = 3$–4.5 where ultrarelativistic electrons depleted. On the other hand, for the nongeoeffective event, depletion occurred from seed to ultrarelativistic energies, except at $L = 3.5$–4 where fluxes at all these energies were enhanced, in particular at seed and relativistic energies.

It is however important to note that the overall response should be interpreted with caution as it does not take into account the variations within the sheath that can be significant. For example, the response parameter misses the strong enhancement at ultrarelativistic energies that occurred during the beginning of the sheath at $L = 4$–5 in the nongeoeffective event (Figure 4ii, panel d) and only records the post-sheath depletion as compared to the pre-sheath levels. This initial brief enhancement was likely associated with the interplanetary shock impact that can quickly accelerate ultrarelativistic electrons via compression induced electric fields and drift resonant acceleration by related ULF waves (e.g., Kanekal et al., 2016; Hao et al., 2019). The response parameter calculated over short timescales (6 h) nevertheless reveals the outer belt electron flux variation in response to specific driver structures, as opposed to studies investigating considerably longer time periods (e.g., Reeves et al., 2003; Turner et al., 2015, 2019).

The analysis of electron fluxes and phase space density (PSD) for different Van Allen Probes orbits allowed for gaining more information of changes in the outer radiation belt during the sheath and insight into processes that govern the electron dynamics. The behaviour of relativistic $\mu = 300$ MeV/G electrons during the sheath was drastically different between the two events. For Event 1, PSD enhanced at all probed L^* after a mild initial depletion, while PSD during Event 2 enhanced only at lower L^* and decreased at higher L^*. As was mentioned in Section 3.4, the PSD behaviour of $\mu = 300$ MeV/G electrons for Event 2 evidenced the effective magnetopause shadowing resulting from the combined process of magnetopause inward incursion and radial diffusion (Turner, Shprits, et al., 2012; Turner & Ukhorskiy, 2020). In addition, the most distinct variations of $\mu = 300$ MeV/G PSD occurred in different parts of the sheath for Event 1 and Event 2. These differences in lower energy response and timing of dynamics can be largely related to different levels of substorm activity and different solar wind dynamic pressure profiles that caused the magnetopause compression and ULF activity to peak in different parts of the sheath. The dynamic pressure, and consequentially the strongest magnetopause incursion and ULF Pc5 activity, occurred just after the shock in Event 1, while for Event 2 they occurred in the latter part of the sheath. Substorm injections producing a sufficiently enhanced seed population during Event 1 also enabled the subsequent enhancements at core and ultrarelativistic energies (Boyd et al., 2016).

Lower energy electrons ($\mu = 300$ MeV/G) did not deplete significantly at the start of the sheath in Event 1 despite the magnetopause incursion, as opposed to higher energy electrons. This could be related to strong substorm activity quickly replenishing lower energy electrons and to their slower drift times about the Earth (from tens of minutes to more than an hour, compared to minutes for ultrarelativistic electrons in the heart of the belt) combined with the briefness of the strongest magnetopause compression. The significant PSD enhancement after this initial light depletion is likely related to strong substorm activity continuing injecting electrons, and fast ULF wave driven inward radial diffusion, as well as the magnetopause relaxing toward a more nominal position. The evolution of the PSD gradient especially during the latter part of the sheath suggests the existence of an increasing source population at higher L^* (Chen, Reeves, & Friedel, 2007).

We note that the level of magnetopause compression and ULF wave activity was similar between the two events. The geoeffective event however resulted in significant substorm injections and a growing source population at high L^* that dominated over losses at the magnetopause and led to a drastically different response of $\mu = 300$ MeV/G electrons as compared to the nongeoeffective event.

Ultrarelativistic electron PSD ($\mu = 3000$ MeV/G) showed also very distinct responses between the studied events. For Event 2, high energy electrons evidenced a very similar response as lower energy electrons, i.e., effective magnetopause shadowing. The initial strong enhancement at ultrarelativistic energies seen in the electron fluxes is not noticeable in the PSD profiles (Figure 6ii, panel b) due to the lack of PSD measurements at $L^* > 4$ before the enhancement. The PSD profiles for Event 1 presented also a similar loss process during the closest magnetopause incursion just after the shock, but the geoeffective event experienced a very different response during the latter part of the sheath and ejecta, as described below. We note that the solar wind conditions in Event 1 follow the three criteria of Li et al. (2015) for efficient MeV electron acceleration. Event 1 had prolonged southward Bz during the sheath, high solar wind speed and PSD enhanced only after the dynamic pressure dropped to low values. This allowed the magnetopause to relax, leading to decreased magnetopause shadowing losses, while the elevated dynamic pressure throughout the sheath of Event 2 caused persistent losses via magnetopause shadowing.

A particularly distinct feature for high energy $\mu = 3000$ MeV/G PSD for Event 1 is the development of a peak. A local peak is usually taken as evidence for local acceleration by chorus waves. The chorus proxy suggests these waves were present throughout the sheath, and the activity also intensified at the time when the peak grew strongly. The chorus activity was spread along a wide range of L, but was strongest around the radial location of the PSD peak. The peak was observed at $L^* = 4.6$–5 and it appeared near the middle of the sheath. The peak grew three orders of magnitude in ~ 12 hours. Local peaks near $L^* = 4$–5 have been commonly observed in previous studies (e.g., Green & Kivelson, 2004; Reeves et al., 2013; Turner, Angelopoulos, Li, et al., 2014; Kanekal et al., 2015; Li et al., 2014, 2016). Similar peak growth rate as in our study was observed by Reeves et al. (2013), which was interpreted to have arisen due to local acceleration by chorus waves by Thorne et al. (2013). Slower growth rates of about two orders of magnitude in $\sim$ 12 hours and about four orders of magnitude in $\sim$ 2 days were observed by Li et al. (2014) and Li et al. (2016), respectively, and both concluded using diffusion simulations that chorus was the dominant cause for acceleration to MeV energies.

However, ambiguity arises for the mechanism generating the PSD peak in Event 1 due to the limited Van Allen Probes measurements beyond $L^* = 5$, and due to peak growth solely recorded by a single pass by Van Allen Probe A without confirmation from Van Allen Probe B. One possible explanation is chorus acceleration beyond the Van Allen Probes' apogee for lower energy electrons that get further energized when transported inward to the peak location by ULF waves, i.e., the peak is not necessarily fully generated by local chorus acceleration at $L^* = 4.6$–5. However, the existence of a local peak in Event 1 has been confirmed by THEMIS spacecraft measurements beyond Van Allen Probes' apogee by Boyd et al. (2018), who also found local acceleration to be the typical cause for energization at MeV energies. In addition, since the peak retains its shape and magnitude for at least 12 hours, there must be an active source to balance the ULF-driven radial diffusion that would flatten and broaden the peak. This would be from local acceleration or a sustained source of electrons further out, but there are no indication of inward radial diffusion. Instead, the peak is slowly transported outwards during the ejecta which is consistent with typical recovery where chorus acceleration moves to higher L-shells.

There is another interesting feature in the PSD profiles of the geoeffective event at $\mu = 3000$ MeV/G: a dip in PSD at $L^* = 3$–3.6, which suggest a local loss. Considering both the PSD and electron fluxes, clearly the strongest depletion of the ultrarelativistic population at low L ($L \sim 3.5$) occurred at 6–10 UT on 2 October ($\sim$18–23 MLT for RBSP-A and for RBSP-B from ~ 22 MLT through a quick pass to early afternoon hours). Such depletions at low L for ultrarelativistic energies are commonly reported in previous studies (e.g., Turner et al., 2013; Turner, Angelopoulos, Li, et al., 2014; Turner, Angelopoulos, Morley, et al., 2014; Aseev et al., 2017), but their causes have remained uncertain. The depletion occurred when the inner magnetospheric wave activity was intense (Pc5, EMIC, chorus and hiss waves). In particular, Van Allen Probe A passed through the evening sector and was outside the plasmasphere, making wave-scattering losses by EMIC waves a possible cause (Aseev et al., 2017; Shprits et al., 2017). This can be as fast as hours for the ultrarelativistic population (e.g., Kurita et al., 2018). Another mechanism that has been invoked to deplete ultrarelativistic fluxes quickly throughout the outer belt is the combined effect of magnetopause incursion, ULF wave transport and drift-shell splitting (Zhang et al., 2016). The speed of the depletion and the fact that the magnetopause was at this time already considerably relaxed makes the former scenario more likely.

It is also interesting to note that a three-part radiation belt structure for ultrarelativistic electrons (4.2 MeV, Figure 4) was created as a response to the sheath region of the geoeffective event, i.e., the outer belt split into two parts (Baker, Kanekal, Hoxie, Batiste, et al., 2013; Turner et al., 2013; Pinto et al., 2018). For the nongeoeffective event, in turn, a pre-existing two-part outer belt structure disappeared leaving only the remnant belt. For the geoeffective event, part of the intense remnant belt that was present before the shock/sheath arrival remained through the sheath despite suffering a considerable depletion at the start of the sheath and a further smaller depletion at the trailing part of the sheath. The largest L-shells of the outer belt captured by Van Allen Probes were largely devoid of ultrarelativistic electrons from the pre-event until the end of the sheath, after which fresh ultrarelativistic electrons appeared. The region $L \sim 4$ remained however devoid of electrons producing the two-part outer belt structure. For the nongeoeffective event, the disappearance of a two-part outer belt structure was caused by two processes, as indicated by the PSD analysis. First, ULF wave related inward transport filled the existing gap between the two bands of enhanced fluxes (remnant belt at $L = 3.5$–4 and an outer belt at $L > 4.5$) that were present before the event. Second, electrons were removed from high L-shells by magnetopause shadowing and outward transport by ULF waves without much further energization, leaving only the remnant belt.

This study highlights that regions close to the shock and ejecta leading edge seem to be key periods when changes in the radiation belt system occur, including most enhanced precipitation from the radiation belts. The major variations of outer belt electron fluxes, both depletion and enhancement, were observed under the influence of these regions. The statistical study of Kalliokoski et al. (2020) showed that the AL index dips after the shock for all sheath events and dips close to the ejecta leading edge for all geoeffective sheaths, indicating intense substorm activity in these key regions. Kilpua et al. (2019) similarly found that regions near the start and end of a sheath are the most geoeffective. These regions also exhibit enhanced ULF wave activity (Kilpua et al., 2013).

Additionally, this study indicated that the chorus proxy based on electron precipitation was important for capturing the chorus wave activity. For both of the studied events, the Van Allen Probes spent little time in the dawn sector where chorus waves typically occur. The chorus proxy also allowed estimation of the L-range of chorus activity showing that it encompassed the entire outer radiation belt. Some chorus activity was almost continuous throughout the geoeffective event, but the activity peaked strongly in the above described key sheath sub-regions: just after the shock and close to the ejecta leading edge. This is consistent with strong disturbances in the AL index at these times, indicating large substorm activity that would likely generate chorus waves and provide a seed population for ultrarelativistic growth (Miyoshi et al., 2013; Jaynes et al., 2015). These sub-regions showed also the strongest chorus activity for the nongeoeffective event.

5 Conclusions

We studied the effects of two interplanetary coronal mass ejections with sheath regions on the outer radiation belt electrons. The two sheath events were geoeffective (2 October 2013; Event 1) and nongeoeffective (15 February 2014; Event 2) based on the $SYM\text{-}H$ geomagnetic activity index during the sheath, and neither ejecta caused significant geomagnetic disturbances.

Our study highlights that both geoeffective and nongeoeffective drivers caused drastic variations of the outer radiation belt electron fluxes up to ultrarelativistic energies. The overall response of the outer belt to the sheath for the geoeffective and nongeoeffective sheaths were the opposite: the geoeffective event led to enhancement for most of the energies and L-ranges, while the nongeoeffective event mainly resulted in depletion. The overall response however hides some distinct variations. For example, for the nongeoeffective event ultrarelativistic electrons experienced about an order of magnitude increase during the sheath before they depleted.

Analysis of electron phase space density at relativistic and ultrarelativistic energies showed that the enhancement observed during the geoeffective sheath was likely due to substorm injections at lower energies and local acceleration by chorus waves at higher energies. In both events, depletion predominantly occurred via loss to the magnetopause driven by magnetopause compression and outward transport by ULF waves. Local loss at low L-shells in the geoeffective event was likely caused by pitch angle scattering by EMIC waves. These different responses derive from differences in substorm activity during the events and the properties of the two sheaths. The different timing and extent of the solar wind dynamic pressure pulse in the sheath contributed to the timing of the closest magnetopause inward incursion and thus when magnetopause shadowing losses were dominant. The relaxation of the magnetopause early in the geoeffective sheath along with mostly southward interplanetary magnetic field, leading to stronger substorm activity that generated chorus waves, created favorable conditions for energization of ultrarelativistic electrons, as opposed to the nongeoeffective sheath.

The results revealed the importance of ULF wave driven inward and outward radial transport for governing electron dynamics, together with the compression of the magnetopause. We also noted the existence of key sheath sub-regions, located at the start and end of the sheath, which cause the main variations. An interesting difference between the events was that the geoeffective sheath created a two-part outer belt structure, while the nongeoeffective sheath destroyed such pre-existing configuration.

Additional case studies are needed to determine if there are repeatable patterns in the response processes of the radiation belt system to sheaths. A statistical approach to phase space density analysis could shed light on the dominant electron dynamics (e.g., Turner et al., 2017; Murphy et al., 2018; Zhao et al., 2019; Nasi et al., 2020). Future work will target events after August 2015 when data from the Magnetospheric Multiscale Mission (MMS) is available. The orbit of MMS allows investigation of PSD distributions beyond Van Allen Probes' apogee eliminating the ambiguity of PSD gradients near geosynchronous orbit (e.g., Cohen et al., 2021).

Acknowledgments

The authors are thankful to all of the Van Allen Probes, Wind, and OMNI teams for making their data available to the public. The OMNI and Wind data were obtained through CDAWeb (`https://cdaweb.sci.gsfc.nasa.gov/index.html/`). We thank Harlan Spence and the ECT team for Van Allen Probes MagEIS and REPT electron flux data (`https://rbsp-ect.lanl.gov/science/DataDirectories.php`) and Craig Kletzing and the EMFISIS team for Van Allen Probes wave data (`https://emfisis.physics.uiowa.edu/data/index`). POES data is available through NOAA (`https://www.ngdc.noaa.gov/stp/satellite/poes/dataaccess.html`) and we thank Timo Asikainen for providing the processed POES data which were obtained through the PROSPECT project (Academy of Finland grant 321440). The results presented here have been achieved under the framework of the Finnish Centre of Excellence in Research of Sustainable Space (Academy of Finland grant 1312390), which we gratefully acknowledge. E. K. acknowledges the European Research Council (ERC) under the European Union's Horizon 2020 Research and Innovation Programme Project SolMAG 724391, and Academy of Finland project 1310445. The work of L. T. is supported by the Academy of Finland (grant 322544). M. P. acknowledges ERC under the European Union's Horizon 2020 Research and Innovation Programme Project 682068-PRESTISSIMO, and Academy of Finland project 312351.

References

Alves, L. R., Da Silva, L. A., Souza, V. M., Sibeck, D. G., Jauer, P. R., Vieira, L. E. A., … Kletzing, C. A. (2016, February). Outer radiation belt dropout dynamics following the arrival of two interplanetary coronal mass ejections. *Geophys. Res. Lett.*, *43*, 978-987. doi: 10.1002/2015GL067066

Anderson, B. R., Millan, R. M., Reeves, G. D., & Friedel, R. H. W. (2015, Dec). Acceleration and loss of relativistic electrons during small geomagnetic storms. *Geophys. Res. Lett.*, *42*(23), 10,113-10,119. doi: 10.1002/2015GL066376

Aseev, N. A., Shprits, Y. Y., Drozdov, A. Y., Kellerman, A. C., Usanova, M. E., Wang, D., & Zhelavskaya, I. S. (2017, October). Signatures of Ultrarelativistic Electron Loss in the Heart of the Outer Radiation Belt Measured by Van Allen Probes. *J. Geophys. Res. Space Physics*, *122*(10), 10,102-10,111. doi: 10.1002/2017JA024485

Asikainen, T. (2017). Calibrated and corrected POES/MEPED energetic particle observations. In Belehaki, A., Hapgood, M. and Watermann, J. (Ed.), *The ESPAS e-infrastructure: Access to data in near-Earth space* (p. 57-69). EDP Science. doi: 10.1051/978-2-7598-1949-2

Asikainen, T., & Mursula, K. (2013, October). Correcting the NOAA/MEPED energetic electron fluxes for detector efficiency and proton contamination. *J. Geophys. Res. Space Physics*, *118*(10), 6500-6510. doi: 10.1002/jgra.50584

Baker, D. N., Kanekal, S. G., Hoxie, V. C., Batiste, S., Bolton, M., Li, X., … Friedel, R. (2013, Nov). The Relativistic Electron-Proton Telescope (REPT) Instrument on Board the Radiation Belt Storm Probes (RBSP) Spacecraft: Characterization of Earth's Radiation Belt High-Energy Particle Populations. *Space Sci. Rev.*, *179*(1-4), 337-381. doi: 10.1007/s11214-012-9950-9

Baker, D. N., Kanekal, S. G., Hoxie, V. C., Henderson, M. G., Li, X., Spence, H. E., … Claudepierre, S. G. (2013, Apr). A Long-Lived Relativistic Electron Storage Ring Embedded in Earth's Outer Van Allen Belt. *Science*, *340*(6129), 186-190. doi: 10.1126/science.1233518

Blake, J. B., Carranza, P. A., Claudepierre, S. G., Clemmons, J. H., Crain, W. R., Dotan, Y., … Zakrzewski, M. P. (2013, Nov). The Magnetic Electron Ion Spectrometer (MagEIS) Instruments Aboard the Radiation Belt Storm Probes (RBSP) Spacecraft. *Space Sci. Rev.*, *179*(1-4), 383-421. doi: 10.1007/s11214-013-9991-8

Bortnik, J., & Thorne, R. M. (2007, Mar). The dual role of ELF/VLF chorus waves in the acceleration and precipitation of radiation belt electrons. *Journal of Atmospheric and Solar-Terrestrial Physics*, *69*(3), 378-386. doi: 10.1016/j.jastp.2006.05.030

Boyd, A. J., Spence, H. E., Claudepierre, S. G., Fennell, J. F., Blake, J. B., Baker, D. N., … Turner, D. L. (2014, April). Quantifying the radiation belt seed population in the 17 March 2013 electron acceleration event. *Geophys. Res. Lett.*, *41*(7), 2275-2281. doi: 10.1002/2014GL059626

Boyd, A. J., Spence, H. E., Huang, C. L., Reeves, G. D., Baker, D. N., Turner, D. L., … Shprits, Y. Y. (2016, August). Statistical properties of the radiation belt seed population. *J. Geophys. Res. Space Physics*, *121*(8), 7636-7646. doi: 10.1002/2016JA022652

Boyd, A. J., Turner, D. L., Reeves, G. D., Spence, H. E., Baker, D. N., & Blake, J. B. (2018, June). What Causes Radiation Belt Enhancements: A Survey of the Van Allen Probes Era. *Geophys. Res. Lett.*, *45*(11), 5253-5259. doi: 10.1029/2018GL077699

Burtis, W. J., & Helliwell, R. A. (1969, Jan). Banded chorus—A new type of VLF radiation observed in the magnetosphere by OGO 1 and OGO 3. *J. Geophys. Res.*, *74*(11), 3002. doi: 10.1029/JA074i011p03002

Chen, Y., Friedel, R. H. W., Reeves, G. D., Cayton, T. E., & Christensen, R. (2007, November). Multisatellite determination of the relativistic electron phase space density at geosynchronous orbit: An integrated investigation during geomagnetic storm times. *J. Geophys. Res. Space Physics*, *112*(A11), A11214. doi: 10.1029/2007JA012314

Chen, Y., Friedel, R. H. W., Reeves, G. D., Onsager, T. G., & Thomsen, M. F. (2005, Oct). Multisatellite determination of the relativistic electron phase space density at geosynchronous orbit: Methodology and results during geomagnetically quiet times. *J. Geophys. Res. Space Physics*, *110*(A10), A10210. doi: 10.1029/2004JA010895

Chen, Y., Reeves, G. D., & Friedel, R. H. W. (2007, Sep). The energization of relativistic electrons in the outer Van Allen radiation belt. *Nat. Phys.*, *3*(9), 614-617. doi: 10.1038/nphys655

Chen, Y., Reeves, G. D., Friedel, R. H. W., & Cunningham, G. S. (2014, February). Global time-dependent chorus maps from low-Earth-orbit electron precipitation and Van Allen Probes data. *Geophys. Res. Lett.*, *41*(3), 755-761. doi: 10.1002/2013GL059181

Claudepierre, S. G., O'Brien, T. P., Blake, J. B., Fennell, J. F., Roeder, J. L., Clemmons, J. H., … Larsen, B. A. (2015, Jul). A background correction algorithm for Van Allen Probes MagEIS electron flux measurements. *J. Geophys. Res. Space Physics*, *120*(7), 5703-5727. doi: 10.1002/2015JA021171

Cohen, I. J., Turner, D. L., Michael, A. T., Sorathia, K. A., & Ukhorskiy, A. Y. (2021). Investigating the Link Between Outer Radiation Belt Losses and Energetic Electron Escape at the Magnetopause: A Case Study Using Multi-Mission Observations and Simulations. *J. Geophys. Res. Space Physics*, *126*(6), e2021JA029261. doi: 10.1029/2021JA029261

Da Silva, L. A., Shi, J., Alves, L. R., Sibeck, D., Souza, V. M., Marchezi, J. P., … Kanekal, S. G. (2020). Dynamic Mechanisms Associated With High-Energy Electron Flux Dropout in the Earth's Outer Radiation Belt Under the Influence of a Coronal Mass Ejection Sheath Region. *J. Geophys. Res. Space Physics*, *126*(1), e2020JA028492. Retrieved from `https://agupubs.onlinelibrary.wiley.com/doi/abs/10.1029/2020JA028492` doi: 10.1029/2020JA028492

Engebretson, M. J., Posch, J. L., Braun, D. J., Li, W., Ma, Q., Kellerman, A. C., … Ermakova, E. (2018, Aug). EMIC Wave Events During the Four GEM QARBM Challenge Intervals. *J. Geophys. Res. Space Physics*, *123*(8), 6394-6423. doi: 10.1029/2018JA025505

Evans, D. S., & Greer, M. S. (2004, January). *Polar orbiting environmental satellite space environment monitor – 2: Instrument descriptions and archive data documentation* (Tech. Rep. No. version 1.4). Boulder, Colorado: Space Environment Center.

George, H., Kilpua, E., Osmane, A., Asikainen, T., Kalliokoski, M. M. H., Rodger, C. J., ... Palmroth, M. (2020, August). Outer Van Allen belt trapped and precipitating electron flux responses to two interplanetary magnetic clouds of opposite polarity. *Ann. Geophys.*, *38*(4), 931-951. doi: 10.5194/angeo-38-931-2020

Georgiou, M., Daglis, I. A., Rae, I. J., Zesta, E., Sibeck, D. G., Mann, I. R., ... Tsinganos, K. (2018, Dec). Ultralow Frequency Waves as an Intermediary for Solar Wind Energy Input Into the Radiation Belts. *J. Geophys. Res. Space Physics*, *123*(12), 10,090-10,108. doi: 10.1029/2018JA025355

Gonzalez, W. D., Joselyn, J. A., Kamide, Y., Kroehl, H. W., Rostoker, G., Tsurutani, B. T., & Vasyliunas, V. M. (1994, Apr). What is a geomagnetic storm? *J. Geophys. Res.*, *99*(A4), 5771-5792. doi: 10.1029/93JA02867

Green, J. C. (2006, Jan). Using Electron Phase Space Density Signatures to Identify the Electromagnetic Waves Responsible for Accelerating Relativistic Electrons in Earth's Magnetosphere. In *Magnetospheric ulf waves: Synthesis and new directions* (Vol. 169, p. 225). doi: 10.1029/169GM15

Green, J. C., & Kivelson, M. G. (2001, Nov). A tale of two theories: How the adiabatic response and ULF waves affect relativistic electrons. *J. Geophys. Res.*, *106*(A11), 25777-25792. doi: 10.1029/2001JA000054

Green, J. C., & Kivelson, M. G. (2004, Mar). Relativistic electrons in the outer radiation belt: Differentiating between acceleration mechanisms. *J. Geophys. Res. Space Physics*, *109*(A3), A03213. doi: 10.1029/2003JA010153

Hao, Y. X., Zong, Q. G., Zhou, X. Z., Rankin, R., Chen, X. R., Liu, Y., ... Claudepierre, S. G. (2019, March). Global-Scale ULF Waves Associated With SSC Accelerate Magnetospheric Ultrarelativistic Electrons. *J. Geophys. Res. Space Physics*, *124*(3), 1525-1538. doi: 10.1029/2018JA026134

Hargreaves, J. K., Birch, M. J., & Evans, D. S. (2010, May). On the fine structure of medium energy electron fluxes in the auroral zone and related effects in the ionospheric D-region. *Ann. Geophys.*, *28*(5), 1107-1120. doi: 10.5194/angeo-28-1107-2010

Hartley, D. P., & Denton, M. H. (2014, December). Solving the radiation belt riddle. *Astronomy and Geophysics*, *55*(6), 6.17-6.20. doi: 10.1093/astrogeo/atu247

Hietala, H., Kilpua, E. K. J., Turner, D. L., & Angelopoulos, V. (2014, Apr). Depleting effects of ICME-driven sheath regions on the outer electron radiation belt. *Geophys. Res. Lett.*, *41*(7), 2258-2265. doi: 10.1002/2014GL059551

Jacobs, J. A., Kato, Y., Matsushita, S., & Troitskaya, V. A. (1964, Jan). Classification of Geomagnetic Micropulsations. *J. Geophys. Res.*, *69*(1), 180-181. doi: 10.1029/JZ069i001p00180

Jaynes, A. N., Baker, D. N., Singer, H. J., Rodriguez, J. V., Loto'aniu, T. M., Ali, A. F., ... Reeves, G. D. (2015, Sep). Source and seed populations for relativistic electrons: Their roles in radiation belt changes. *J. Geophys. Res. Space Physics*, *120*(9), 7240-7254. doi: 10.1002/2015JA021234

Kalliokoski, M. M. H., Kilpua, E. K. J., Osmane, A., Turner, D. L., Jaynes, A. N., Turc, L., ... Palmroth, M. (2020, June). Outer radiation belt and inner magnetospheric response to sheath regions of coronal mass ejections: a statistical analysis. *Ann. Geophys.*, *38*(3), 683-701. doi: 10.5194/angeo-38-683-2020

Kanekal, S. G., Baker, D. N., Fennell, J. F., Jones, A., Schiller, Q., Richardson, I. G., ... Wygant, J. R. (2016, August). Prompt acceleration of magnetospheric electrons to ultrarelativistic energies by the 17 March 2015 interplanetary shock. *J. Geophys. Res. Space Physics*, *121*(8), 7622-7635. doi: 10.1002/2016JA022596

Kanekal, S. G., Baker, D. N., Henderson, M. G., Li, W., Fennell, J. F., Zheng, Y., ... Kletzing, C. A. (2015, September). Relativistic electron response to the combined magnetospheric impact of a coronal mass ejection overlapping with a high-speed stream: Van Allen Probes observations. *J. Geophys. Res. Space Physics*, *120*(9), 7629-7641. doi: 10.1002/2015JA021395

Kataoka, R., & Miyoshi, Y. (2006, Sep). Flux enhancement of radiation belt electrons during geomagnetic storms driven by coronal mass ejections and corotating interaction regions. *Space Weather*, *4*(9), 09004. doi: 10.1029/2005SW000211

Katsavrias, C., Daglis, I. A., Turner, D. L., Sand berg, I., Papadimitriou, C., Georgiou, M., & Balasis, G. (2015, Dec). Nonstorm loss of relativistic electrons in the outer radiation belt. *Geophys. Res. Lett.*, *42*(24), 10,521-10,530. doi: 10.1002/2015GL066773

Kilpua, E. K. J., Balogh, A., von Steiger, R., & Liu, Y. D. (2017, November). Geo-effective Properties of Solar Transients and Stream Interaction Regions. *Space Sci. Rev.*, *212*, 1271-1314. doi: 10.1007/s11214-017-0411-3

Kilpua, E. K. J., Fontaine, D., Moissard, C., Ala-Lahti, M., Palmerio, E., Yordanova, E., ... Turc, L. (2019, Jul). Solar wind properties and geospace impact of coronal mass ejection-driven sheath regions: Variation and driver dependence. *Space Weather*, *17*(0). doi: 10.1029/2019SW002217

Kilpua, E. K. J., Hietala, H., Koskinen, H. E. J., Fontaine, D., & Turc, L. (2013, Sep). Magnetic field and dynamic pressure ULF fluctuations in coronal-mass-ejection-driven sheath regions. *Ann. Geophys.*, *31*(9), 1559-1567. doi: 10.5194/angeo-31-1559-2013

Kilpua, E. K. J., Hietala, H., Turner, D. L., Koskinen, H. E. J., Pulkkinen, T. I., Rodriguez, J. V., ... Spence, H. E. (2015, May). Unraveling the drivers of the storm time radiation belt response. *Geophys. Res. Lett.*, *42*(9), 3076-3084. doi: 10.1002/2015GL063542

Kilpua, E. K. J., Koskinen, H. E. J., & Pulkkinen, T. I. (2017, Nov). Coronal mass ejections and their sheath regions in interplanetary space. *Living Rev. Sol. Phys.*, *14*(1), 5. doi: 10.1007/s41116-017-0009-6

Kim, H.-J., & Chan, A. A. (1997, September). Fully adiabatic changes in storm time relativistic electron fluxes. *J. Geophys. Res.*, *102*(A10), 22107-22116. doi: 10.1029/97JA01814

Kletzing, C. A., Kurth, W. S., Acuna, M., MacDowall, R. J., Torbert, R. B., Averkamp, T., ... Tyler, J. (2013, Nov). The Electric and Magnetic Field Instrument Suite and Integrated Science (EMFISIS) on RBSP. *Space Sci. Rev.*, *179*(1-4), 127-181. doi: 10.1007/s11214-013-9993-6

Koons, H. C., & Roeder, J. L. (1990, Oct). A survey of equatorial magnetospheric wave activity between 5 and 8 R_E. *Planet. Space Sci.*, *38*(10), 1335-1341. doi: 10.1016/0032-0633(90)90136-E

Kurita, S., Miyoshi, Y., Shiokawa, K., Higashio, N., Mitani, T., Takashima, T., ... Otsuka, Y. (2018, December). Rapid Loss of Relativistic Electrons by EMIC Waves in the Outer Radiation Belt Observed by Arase, Van Allen Probes, and the PWING Ground Stations. *Geophys. Res. Lett.*, *45*(23), 12,720-12,729. doi: 10.1029/2018GL080262

Kurth, W. S., De Pascuale, S., Faden, J. B., Kletzing, C. A., Hospodarsky, G. B., Thaller, S., & Wygant, J. R. (2015, Feb). Electron densities inferred from plasma wave spectra obtained by the Waves instrument on Van Allen Probes. *J. Geophys. Res. Space Physics*, *120*(2), 904-914. doi: 10.1002/2014JA020857

Lam, M. M., Horne, R. B., Meredith, N. P., Glauert, S. A., Moffat-Griffin, T., & Green, J. C. (2010, April). Origin of energetic electron precipitation ¿30 keV into the atmosphere. *J. Geophys. Res. Space Physics*, *115*(8), A00F08. doi: 10.1029/2009JA014619

Lepping, R. P., Acũna, M. H., Burlaga, L. F., Farrell, W. M., Slavin, J. A., Schatten, K. H., ... Worley, E. M. (1995, February). The Wind Magnetic Field Investigation. *Space Sci. Rev.*, *71*, 207-229. doi: 10.1007/BF00751330

Li, W., Ma, Q., Thorne, R. M., Bortnik, J., Zhang, X. J., Li, J., ... Goldstein, J. (2016, June). Radiation belt electron acceleration during the 17 March 2015 geomagnetic storm: Observations and simulations. *J. Geophys. Res. Space Physics*, *121*(6), 5520-5536. doi: 10.1002/2016JA022400

Li, W., Thorne, R. M., Bortnik, J., Baker, D. N., Reeves, G. D., Kanekal, S. G., ... Green, J. C. (2015, September). Solar wind conditions leading to efficient radiation belt electron acceleration: A superposed epoch analysis. *Geophys. Res. Lett.*, *42*(17), 6906-6915. doi: 10.1002/2015GL065342

Li, W., Thorne, R. M., Ma, Q., Ni, B., Bortnik, J., Baker, D. N., ... Claudepierre, S. G. (2014, June). Radiation belt electron acceleration by chorus waves during the 17 March 2013 storm. *J. Geophys. Res. Space Physics*, *119*(6), 4681-4693. doi: 10.1002/2014JA019945

Lugaz, N., Farrugia, C. J., Winslow, R. M., Al-Haddad, N., Kilpua, E. K. J., & Riley, P. (2016, Nov). Factors affecting the geoeffectiveness of shocks and sheaths at 1 AU. *J. Geophys. Res. Space Physics*, *121*(11), 10,861-10,879. doi: 10.1002/2016JA023100

Malaspina, D. M., Ripoll, J.-F., Chu, X., Hospodarsky, G., & Wygant, J. (2018, September). Variation in Plasmaspheric Hiss Wave Power With Plasma Density. *Geophys. Res. Lett.*, *45*(18), 9417-9426. doi: 10.1029/2018GL078564

Masías-Meza, J. J., Dasso, S., Démoulin, P., Rodriguez, L., & Janvier, M. (2016, Aug). Superposed epoch study of ICME sub-structures near Earth and their effects on Galactic cosmic rays. *Astron. Astrophys.*, *592*, A118. doi: 10.1051/0004-6361/201628571

Mauk, B. H., Fox, N. J., Kanekal, S. G., Kessel, R. L., Sibeck, D. G., & Ukhorskiy, A. (2013, Nov). Science Objectives and Rationale for the Radiation Belt Storm Probes Mission. *Space Sci. Rev.*, *179*(1-4), 3-27. doi: 10.1007/s11214-012-9908-y

Miyoshi, Y., Kataoka, R., Kasahara, Y., Kumamoto, A., Nagai, T., & Thomsen, M. F. (2013, September). High-speed solar wind with southward interplanetary magnetic field causes relativistic electron flux enhancement of the outer radiation belt via enhanced condition of whistler waves. *Geophys. Res. Lett.*, *40*(17), 4520-4525. doi: 10.1002/grl.50916

Moissard, C., Fontaine, D., & Savoini, P. (2019, November). A Study of Fluctuations in Magnetic Cloud-Driven Sheaths. *J. Geophys. Res. Space Physics*, *124*(11), 8208-8226. doi: 10.1029/2019JA026952

Morley, S. K., Henderson, M. G., Reeves, G. D., Friedel, R. H. W., & Baker, D. N. (2013, September). Phase Space Density matching of relativistic electrons using the Van Allen Probes: REPT results. *Geophys. Res. Lett.*, *40*(18), 4798-4802. doi: 10.1002/grl.50909

Moya, P. S., Pinto, V. A., Sibeck, D. G., Kanekal, S. G., & Baker, D. N. (2017, Nov). On the Effect of Geomagnetic Storms on Relativistic Electrons in the Outer Radiation Belt: Van Allen Probes Observations. *J. Geophys. Res. Space Physics*, *122*(11), 11,100-11,108. doi: 10.1002/2017JA024735

Murphy, K. R., Watt, C. E. J., Mann, I. R., Jonathan Rae, I., Sibeck, D. G., Boyd, A. J., ... Fennell, J. (2018, May). The Global Statistical Response of the Outer Radiation Belt During Geomagnetic Storms. *Geophys. Res. Lett.*, *45*(9), 3783-3792. doi: 10.1002/2017GL076674

Nasi, A., Daglis, I. A., Katsavrias, C., & Li, W. (2020, November). Interplay of source/seed electrons and wave-particle interactions in producing relativistic electron PSD enhancements in the outer Van Allen belt. *J. Atmos. Solar-Terr. Phys.*, *210*, 105405. doi: 10.1016/j.jastp.2020.105405

O'Brien, T. P., McPherron, R. L., Sornette, D., Reeves, G. D., Friedel, R., & Singer, H. J. (2001, Aug). Which magnetic storms produce relativistic electrons at geosynchronous orbit? *J. Geophys. Res.*, *106*(A8), 15533-15544. doi: 10.1029/2001JA000052

Ogilvie, K. W., Chornay, D. J., Fritzenreiter, R. J., Hunsaker, F., Keller, J., Lobell, J., … Gergin, E. (1995, February). SWE, A Comprehensive Plasma Instrument for the Wind Spacecraft. *Space Sci. Rev.*, *71*, 55-77. doi: 10.1007/BF00751326

Pinto, V. A., Bortnik, J., Moya, P. S., Lyons, L. R., Sibeck, D. G., Kanekal, S. G., … Baker, D. N. (2018, November). Characteristics, Occurrence, and Decay Rates of Remnant Belts Associated With Three-Belt Events in the Earth's Radiation Belts. *Geophys. Res. Lett.*, *45*(22), 12,099-12,107. doi: 10.1029/2018GL080274

Reeves, G. D., McAdams, K. L., Friedel, R. H. W., & O'Brien, T. P. (2003, May). Acceleration and loss of relativistic electrons during geomagnetic storms. *Geophys. Res. Lett.*, *30*(10), 1529. doi: 10.1029/2002GL016513

Reeves, G. D., Spence, H. E., Henderson, M. G., Morley, S. K., Friedel, R. H. W., Funsten, H. O., … Niehof, J. T. (2013, Aug). Electron Acceleration in the Heart of the Van Allen Radiation Belts. *Science*, *341*(6149), 991-994. doi: 10.1126/science.1237743

Richardson, I. G., & Cane, H. V. (2010, Jun). Near-Earth Interplanetary Coronal Mass Ejections During Solar Cycle 23 (1996 - 2009): Catalog and Summary of Properties. *Solar Phys.*, *264*(1), 189-237. doi: 10.1007/s11207-010-9568-6

Rodger, C. J., Carson, B. R., Cummer, S. A., Gamble, R. J., Clilverd, M. A., Green, J. C., … Berthelier, J.-J. (2010, December). Contrasting the efficiency of radiation belt losses caused by ducted and nonducted whistler-mode waves from ground-based transmitters. *J. Geophys. Res. Space Physics*, *115*(A12), A12208. doi: 10.1029/2010JA015880

Rodger, C. J., Kavanagh, A. J., Clilverd, M. A., & Marple, S. R. (2013, December). Comparison between POES energetic electron precipitation observations and riometer absorptions: Implications for determining true precipitation fluxes. *J. Geophys. Res. Space Physics*, *118*(12), 7810-7821. doi: 10.1002/2013JA019439

Roederer, J. G. (1970). *Dynamics of geomagnetically trapped radiation.* Berlin, Heidelberg: Springer-Verlag. doi: 10.1007/978-3-642-49300-3

Schiller, Q., Li, X., Blum, L., Tu, W., Turner, D. L., & Blake, J. B. (2014, Jan). A nonstorm time enhancement of relativistic electrons in the outer radiation belt. *Geophys. Res. Lett.*, *41*(1), 7-12. doi: 10.1002/2013GL058485

Shprits, Y. Y., Kellerman, A., Aseev, N., Drozdov, A. Y., & Michaelis, I. (2017, Feb). Multi-MeV electron loss in the heart of the radiation belts. *Geophys. Res. Lett.*, *44*(3), 1204-1209. doi: 10.1002/2016GL072258

Shprits, Y. Y., Thorne, R. M., Friedel, R., Reeves, G. D., Fennell, J., Baker, D. N., & Kanekal, S. G. (2006, Nov). Outward radial diffusion driven by losses at magnetopause. *J. Geophys. Res. Space Physics*, *111*(A11), A11214. doi: 10.1029/2006JA011657

Shue, J. H., Song, P., Russell, C. T., Steinberg, J. T., Chao, J. K., Zastenker, G., … Detman, T. R. (1998, Aug). Magnetopause location under extreme solar wind conditions. *J. Geophys. Res.*, *103*(A8), 17691-17700. doi: 10.1029/98JA01103

Singer, H., Matheson, L., Grubb, R., Newman, A., & Bouwer, D. (1996, Oct). Monitoring space weather with the GOES magnetometers. In E. R. Washwell (Ed.), *Goes-8 and beyond* (Vol. 2812, p. 299-308). doi: 10.1117/12.254077

Spence, H. E., Reeves, G. D., Baker, D. N., Blake, J. B., Bolton, M., Bourdarie, S., … Thorne, R. M. (2013, November). Science Goals and Overview of the Radiation Belt Storm Probes (RBSP) Energetic Particle, Composition, and Thermal Plasma (ECT) Suite on NASA's Van Allen Probes Mission. *Space Sci. Rev.*, *179*, 311-336. doi: 10.1007/s11214-013-0007-5

Su, Z., Zhu, H., Xiao, F., Zong, Q. G., Zhou, X. Z., Zheng, H., ... Wygant, J. R. (2015, Dec). Ultra-low-frequency wave-driven diffusion of radiation belt relativistic electrons. *Nat. Commun.*, *6*, 10096. doi: 10.1038/ncomms10096

Summers, D., & Thorne, R. M. (2003, April). Relativistic electron pitch-angle scattering by electromagnetic ion cyclotron waves during geomagnetic storms. *J. Geophys. Res. Space Physics*, *108*(A4), 1143. doi: 10.1029/2002JA009489

Thorne, R. M. (2010, Nov). Radiation belt dynamics: The importance of wave-particle interactions. *Geophys. Res. Lett.*, *37*(22), L22107. doi: 10.1029/2010GL044990

Thorne, R. M., Li, W., Ni, B., Ma, Q., Bortnik, J., Chen, L., ... Kanekal, S. G. (2013, December). Rapid local acceleration of relativistic radiation-belt electrons by magnetospheric chorus. *Nature*, *504*(7480), 411-414. doi: 10.1038/nature12889

Tsyganenko, N. A., & Sitnov, M. I. (2005, Mar). Modeling the dynamics of the inner magnetosphere during strong geomagnetic storms. *J. Geophys. Res. Space Physics*, *110*(A3), A03208. doi: 10.1029/2004JA010798

Turner, D. L., Angelopoulos, V., Li, W., Bortnik, J., Ni, B., Ma, Q., ... Rodriguez, J. V. (2014, Mar). Competing source and loss mechanisms due to wave-particle interactions in Earth's outer radiation belt during the 30 September to 3 October 2012 geomagnetic storm. *J. Geophys. Res. Space Physics*, *119*(3), 1960-1979. doi: 10.1002/2014JA019770

Turner, D. L., Angelopoulos, V., Li, W., Hartinger, M. D., Usanova, M., Mann, I. R., ... Shprits, Y. (2013, May). On the storm-time evolution of relativistic electron phase space density in Earth's outer radiation belt. *J. Geophys. Res. Space Physics*, *118*(5), 2196-2212. doi: 10.1002/jgra.50151

Turner, D. L., Angelopoulos, V., Morley, S. K., Henderson, M. G., Reeves, G. D., Li, W., ... Rodriguez, J. V. (2014, March). On the cause and extent of outer radiation belt losses during the 30 September 2012 dropout event. *J. Geophys. Res. Space Physics*, *119*(3), 1530-1540. doi: 10.1002/2013JA019446

Turner, D. L., Angelopoulos, V., Shprits, Y., Kellerman, A., Cruce, P., & Larson, D. (2012, May). Radial distributions of equatorial phase space density for outer radiation belt electrons. *Geophys. Res. Lett.*, *39*(9), L09101. doi: 10.1029/2012GL051722

Turner, D. L., Kilpua, E. K. J., Hietala, H., Claudepierre, S. G., O'Brien, T. P., Fennell, J. F., ... Reeves, G. D. (2019, February). The Response of Earth's Electron Radiation Belts to Geomagnetic Storms: Statistics From the Van Allen Probes Era Including Effects From Different Storm Drivers. *J. Geophys. Res. Space Physics*, *124*, 1013-1034. doi: 10.1029/2018JA026066

Turner, D. L., O'Brien, T. P., Fennell, J. F., Claudepierre, S. G., Blake, J. B., Jaynes, A. N., ... Reeves, G. D. (2017, January). Investigating the source of near-relativistic and relativistic electrons in Earth's inner radiation belt. *J. Geophys. Res. Space Physics*, *122*(1), 695-710. doi: 10.1002/2016JA023600

Turner, D. L., O'Brien, T. P., Fennell, J. F., Claudepierre, S. G., Blake, J. B., Kilpua, E. K. J., & Hietala, H. (2015, November). The effects of geomagnetic storms on electrons in Earth's radiation belts. *Geophys. Res. Lett.*, *42*, 9176-9184. doi: 10.1002/2015GL064747

Turner, D. L., Shprits, Y., Hartinger, M., & Angelopoulos, V. (2012, Mar). Explaining sudden losses of outer radiation belt electrons during geomagnetic storms. *Nat. Phys.*, *8*(3), 208-212. doi: 10.1038/nphys2185

Turner, D. L., & Ukhorskiy, A. Y. (2020). Chapter 1 - Outer radiation belt losses by magnetopause incursions and outward radial transport: new insight and outstanding questions from the Van Allen Probes era. In A. N. Jaynes & M. E. Usanova (Eds.), *The Dynamic Loss of Earth's Radiation Belts* (p. 1-28). Elsevier. Retrieved from `http://www.sciencedirect.com/science/article/pii/B9780128133712000019` doi: 10.1016/B978-0-12-813371-2.00001-9

Yermolaev, Y. I., Lodkina, I. G., Nikolaeva, N. S., & Yermolaev, M. Y. (2015, September). Dynamics of large-scale solar wind streams obtained by the double superposed epoch analysis. *J. Geophys. Res. Space Physics*, *120*(9), 7094-7106. doi: 10.1002/2015JA021274

Yermolaev, Y. I., Lodkina, I. G., Nikolaeva, N. S., & Yermolaev, M. Y. (2017, December). Dynamics of Large-Scale Solar-Wind Streams Obtained by the Double Superposed Epoch Analysis: 2. Comparisons of CIRs vs. Sheaths and MCs vs. Ejecta. *Solar Phys.*, *292*(12), 193. doi: 10.1007/s11207-017-1205-1

Yermolaev, Y. I., Lodkina, I. G., Nikolaeva, N. S., Yermolaev, M. Y., Riazantseva, M. O., & Rakhmanova, L. S. (2018, November). Statistic study of the geoeffectiveness of compression regions CIRs and Sheaths. *J. Atmos. Solar-Terr. Phys.*, *180*, 52-59. doi: 10.1016/j.jastp.2018.01.027

Zhang, X. J., Li, W., Thorne, R. M., Angelopoulos, V., Ma, Q., Li, J., … Fennell, J. F. (2016, September). Physical mechanism causing rapid changes in ultrarelativistic electron pitch angle distributions right after a shock arrival: Evaluation of an electron dropout event. *J. Geophys. Res. Space Physics*, *121*(9), 8300-8316. doi: 10.1002/2016JA022517

Zhao, H., Baker, D. N., Li, X., Malaspina, D. M., Jaynes, A. N., & Kanekal, S. G. (2019, November). On the Acceleration Mechanism of Ultrarelativistic Electrons in the Center of the Outer Radiation Belt: A Statistical Study. *J. Geophys. Res. Space Physics*, *124*(11), 8590-8599. doi: 10.1029/2019JA027111

Journal of Geophysical Research Space Physics

Supporting Information for

Phase Space Density Analysis of Outer Radiation Belt Electron Energization and Loss during Geoeffective and Nongeoeffective Sheath Regions

Milla M. H. Kalliokoski[1], Emilia K. J. Kilpua[1], Adnane Osmane[1], Allison N. Jaynes[2], Drew L. Turner[3], Harriet George[1], Lucile Turc[1], Minna Palmroth[1,4]

[1]Department of Physics, University of Helsinki, Helsinki, Finland

[2]Department of Physics and Astronomy, University of Iowa, Iowa City, Iowa, USA

[3]Johns Hopkins University Applied Physics Laboratory, Laurel, Maryland, USA

[4]Space and Earth Observation Centre, Finnish Meteorological Institute, Helsinki, Finland

Contents of this file

Figures S1 to S2

Additional Supporting Information (Files uploaded separately)

Captions for Movies S1 to S4

Introduction

The figures presented here show additional data to complement the figures of the main article. We show wave measurements from different spacecraft and the unbinned phase space density (PSD) radial profiles. In addition, we list here the captions for movies of the PSD radial profiles showing more explicitly the time evolution of the profiles. The movies are uploaded separately.

Movie S1. PSD profiles from pass to pass for μ = (300 ± 10) MeV/G in Event 1 (2 October 2013), corresponding to Figure 6i, panel a, in the main article. The current pass is shown in full color with its time indicated by the white triangle in the colorbar, and previous passes are shown faded out. The pass label is shown on the bottom right, indicating whether data for that pass is from the inbound or outbound part of the orbit of Van Allen Probe A or B.

Movie S2. PSD profiles from pass to pass for μ = (3000 ± 10) MeV/G in Event 1 (2 October 2013), corresponding to Figure 6i, panel b, in the main article.

Movie S3. PSD profiles from pass to pass for μ = (300 ± 10) MeV/G in Event 2 (15 February 2014), corresponding to Figure 6ii, panel a, in the main article.

Movie S4. PSD profiles from pass to pass for μ = (3000 ± 10) MeV/G in Event 2 (15 February 2014), corresponding to Figure 6ii, panel b, in the main article.

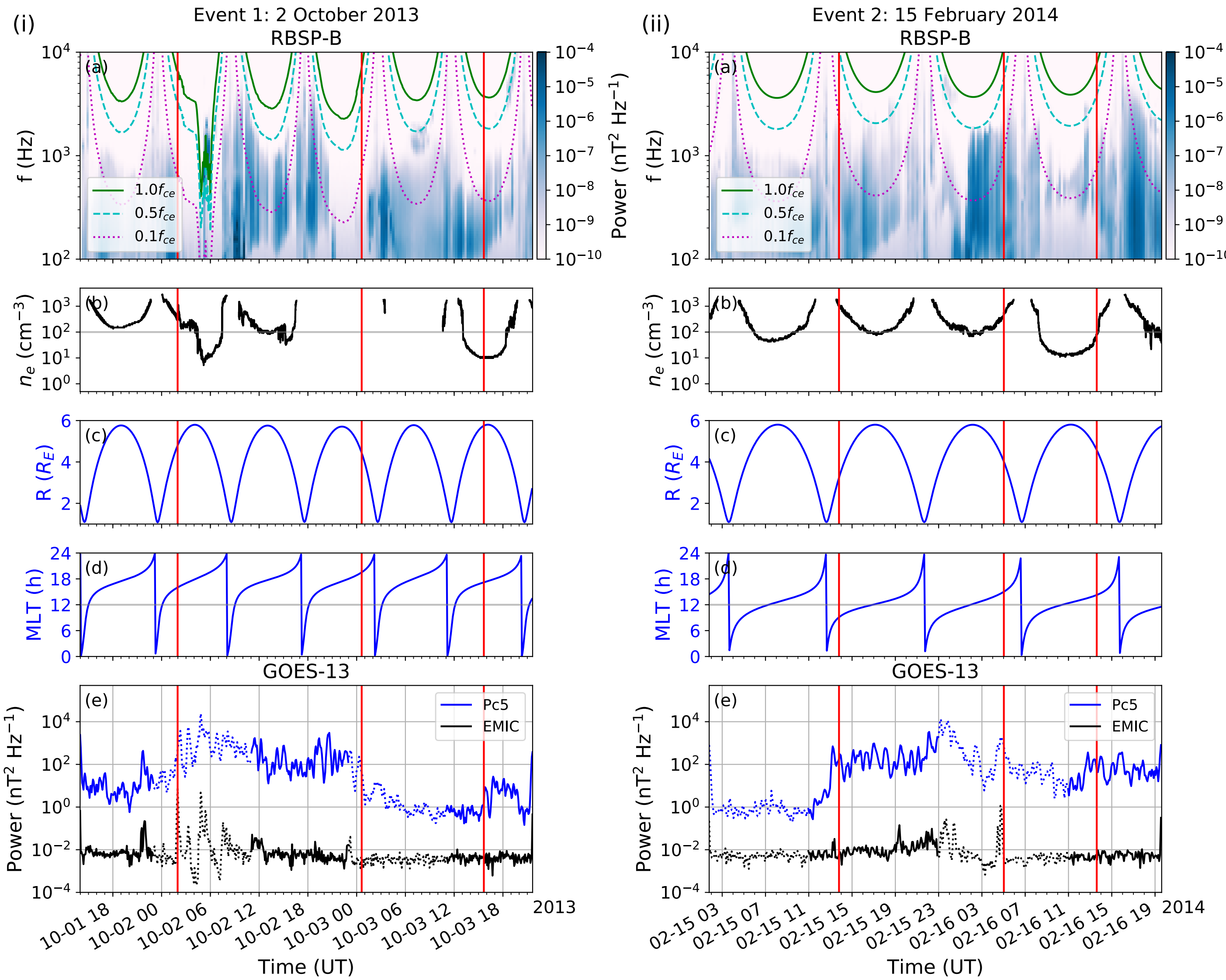

Figure S1. Same as Figure 2 in the main article but showing VLF wave activity measured by Van Allen Probe B and ULF wave powers from GOES-13.

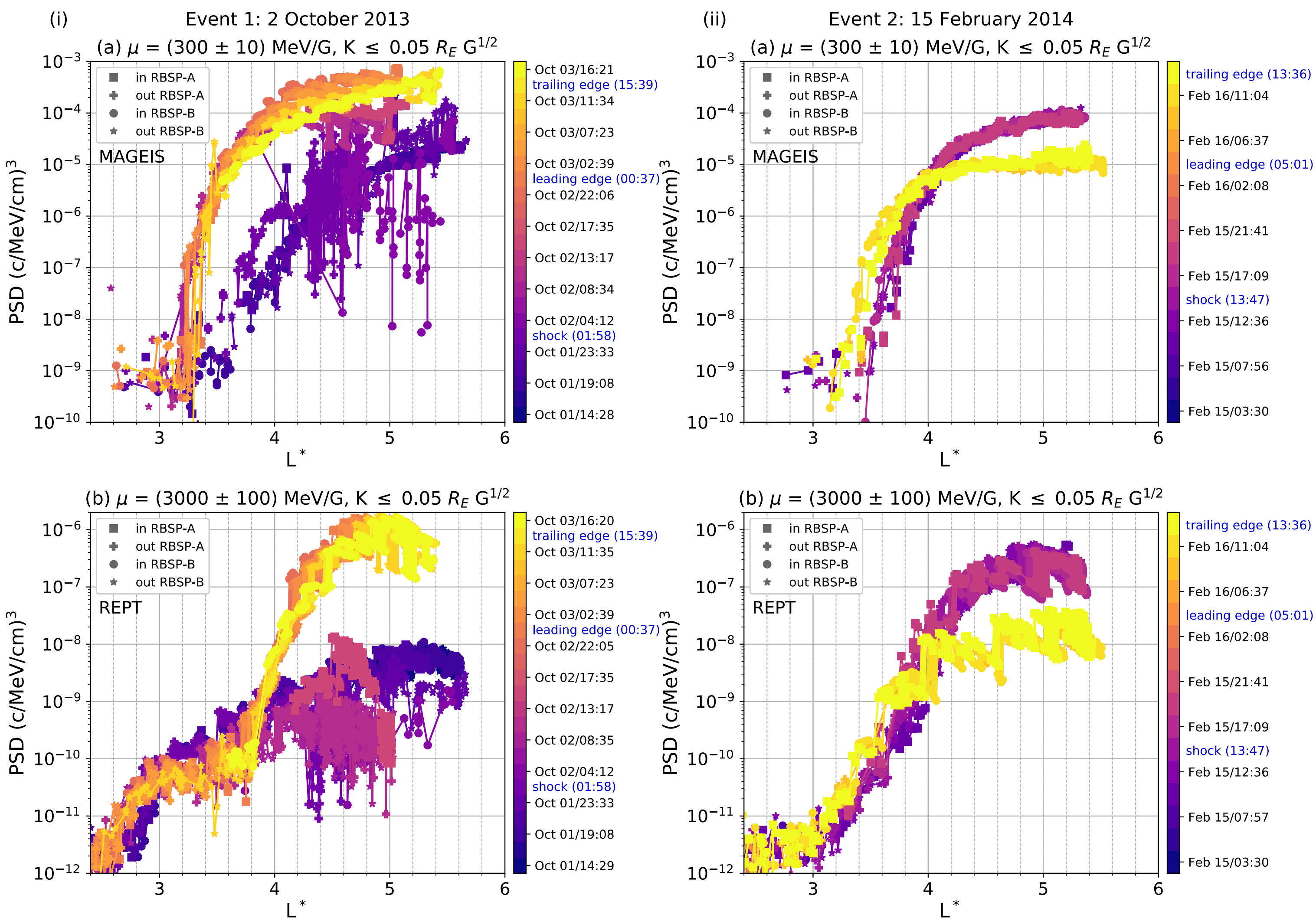

Figure S2. Same as Figure 6 in the main article except the PSD profiles have not been averaged in *L** to smooth them. Fluctuations that originate from finding PSD points corresponding to the chosen ranges of μ and K at multiple energy channels at similar *L** are visible.